870–890 *Nucleic Acids Research, 2023, Vol. 51, No. 2* *Published online 9 January 2023*
https://doi.org/10.1093/nar/gkac1225

Poison cassette exon splicing of *SRSF6* regulates nuclear speckle dispersal and the response to hypoxia

Camila de Oliveira Freitas Machado[1,2], Michal Schafranek[1], Mirko Brüggemann[1,3], María Clara Hernández Cañás[1], Mario Keller[1,3], Antonella Di Liddo[3], Andre Brezski[1,3], Nicole Blümel[1], Benjamin Arnold[1], Anja Bremm[4], Ilka Wittig[5], Nicolas Jaé[2], François McNicoll[1], Stefanie Dimmeler[2], Kathi Zarnack[1,3,*] and Michaela Müller-McNicoll[1,*]

[1]Institute of Molecular Biosciences, Goethe University, Frankfurt am Main, Germany, [2]Institute of Cardiovascular Regeneration, Goethe University, Frankfurt am Main, Germany, [3]Buchmann Institute for Molecular Life Sciences (BMLS), Frankfurt am Main, Germany, [4]Institute of Biochemistry II, Goethe University, Frankfurt am Main, Germany and [5]Functional Proteomics, Institute of Cardiovascular Physiology, Goethe University, Frankfurt am Main, Germany

Received March 10, 2022; Revised December 06, 2022; Editorial Decision December 06, 2022; Accepted December 10, 2022

ABSTRACT

Hypoxia induces massive changes in alternative splicing (AS) to adapt cells to the lack of oxygen. Here, we identify the splicing factor SRSF6 as a key factor in the AS response to hypoxia. The SRSF6 level is strongly reduced in acute hypoxia, which serves a dual purpose: it allows for exon skipping and triggers the dispersal of nuclear speckles. Our data suggest that cells use dispersal of nuclear speckles to reprogram their gene expression during hypoxic adaptation and that SRSF6 plays an important role in cohesion of nuclear speckles. Down-regulation of SRSF6 is achieved through inclusion of a poison cassette exon (PCE) promoted by SRSF4. Removing the PCE 3′ splice site using CRISPR/Cas9 abolishes SRSF6 reduction in hypoxia. Aberrantly high SRSF6 levels in hypoxia attenuate hypoxia-mediated AS and impair dispersal of nuclear speckles. As a consequence, proliferation and genomic instability are increased, while the stress response is suppressed. The SRSF4–PCE–SRSF6 hypoxia axis is active in different cancer types, and high SRSF6 expression in hypoxic tumors correlates with a poor prognosis. We propose that the ultra-conserved PCE of SRSF6 acts as a tumor suppressor and that its inclusion in hypoxia is crucial to reduce SRSF6 levels. This may prevent tumor cells from entering the metastatic route of hypoxia adaptation.

INTRODUCTION

Solid tumors often contain hypoxic microdomains with low concentrations of oxygen. Hypoxia triggers several response mechanisms that enable tumor cells to adapt to low oxygen and nutrient starvation, or to escape from this anaerobic environment, and also confer resistance to chemotherapy (1,2). Signaling pathways are induced to coordinate adaptive processes such as glycolysis, angiogenesis, proliferation, survival and metastasis. Mammalian cells sense oxygen availability through several stress response pathways. Best studied is the transcriptional response via the hypoxia-inducible factors (HIFs) (1,3–6). The HIF1α subunit, which is normally degraded in the cytoplasm, is stabilized by low oxygen levels and imported into the nucleus. There, it forms a dimeric complex with the constitutively expressed HIF1β subunit and, together, they promote the transcription of hundreds of target genes (7). One of the main HIF target transcripts is *vascular endothelial growth factor A* (*VEGFA*). The encoded protein VEGFA is secreted by hypoxic tumors to stimulate growth and migration of endothelial cells, leading to the formation of new blood vessels (5).

Beyond the transcriptional response, recent studies uncovered alternative splicing (AS) as a parallel layer of gene regulation that is important for the adaptation of cancer cells to hypoxia (8–13) and that has emerged as a potent driving force of tumor pathogenesis and progression (14). For example, *VEGFA* pre-mRNA produces several alternatively spliced isoforms with either pro- or anti-angiogenic potential (15). Specific circular transcripts (circRNAs) derived from back-splicing increase in hypoxia, some of which promote angiogenesis (16,17). Furthermore, retention of an intron in the transcript encoding eukaryotic translation ini-

*To whom correspondence should be addressed. Email: mueller-mcnicoll@bio.uni-frankfurt.de
Correspondence may also be addressed to Kathi Zarnack. Email: kathi.zarnack@bmls.de

tiation factor 2B5 (*EIF2B5*) leads to the generation of a truncated protein isoform which inhibits translation in hypoxia (9). The identification of novel splice isoforms that promote the adaptation to hypoxia as well as the study of their regulatory mechanisms could reveal interesting molecular targets for new cancer therapies.

SR proteins are essential splicing factors that bind to alternative exons and promote their inclusion into mature mRNAs (18). The SR protein family comprises 12 canonical members (SRSF1–SRSF12) (19) that act redundantly in constitutive splicing (except SRSF10) but non-redundantly in AS (20,21). SR proteins are often up-regulated in different cancer types (22) and their overexpression (OE) is sufficient to transform normal cells and cause changes in cancer-related processes, such as angiogenesis, epithelial to mesenchymal transition (EMT) and metastasis (22,23). Individual SR proteins display distinct RNA binding specificities and protein interaction partners, and their splicing activities can be activated or inactivated through differential phosphorylation (24–28). Although SR proteins are generally hyperphosphorylated under hypoxia through increased levels of the CDC-like kinases (CLKs) and SR protein kinases (SRPKs) (8,29), this may increase or decrease their RNA binding specificity or splicing activity. Also, the levels of SR proteins are differentially regulated in hypoxia in a cell type-specific manner (8,9,30). However, the mechanisms by which individual SR proteins affect the hypoxia response and cancer progression need to be described in more detail.

SRSF6 is one of the lesser studied SR proteins. It contains two RNA recognition motifs (RRMs) at its N-terminus and an RS domain rich in arginine and serine dipeptides at its C-terminus. SRSF6 is frequently up-regulated in colorectal, lung, skin and breast cancer, and its levels are positively correlated with more aggressive cancer phenotypes and a poor prognosis (31–35). SRSF6 has been shown to inhibit apoptosis and promote epithelial-to-mesenchymal transition (EMT) and metastasis (33,34,36). Paradoxically, SRSF6 also appears to inhibit tumor angiogenesis by promoting the splicing of anti-angiogenic *VEGFA* isoforms (37), and its extreme overexpression even promotes apoptosis and decreases proliferation of HeLa cells (35). Thus, it remains unclear whether and how SRSF6 regulates AS under hypoxic stress and how its aberrant expression contributes to metastatic progression. Here, we characterize the mechanisms by which SRSF6 achieves this dual function.

MATERIALS AND METHODS

Cell culture of wild-type (WT) and BAC cell lines

HeLa cells were cultivated under humidified conditions at 5% CO_2 and 37°C in Dulbecco's modified Eagle's medium (DMEM) Glutamax Medium (Sigma Aldrich) supplemented with 10% (v/v) heat-inactivated fetal bovine serum (FBS; Thermo Fisher Scientific) and 100 U/ml penicillin–streptomycin (Thermo Fisher Scientific). Bacterial artificial chromosomes (BACs) harboring green fluorescent protein (GFP)-tagged *SRSF6* and *SRSF4* genes were isolated from *Escherichia coli* DH10 cells using the NucleoBond PC 20 kit (Macherey-Nagel). WT HeLa cells were transfected with 1 μg of purified BAC DNA using the Effectene Transfection Reagent (Qiagen). Cells with stably integrated BACs were selected with 500 μg/ml geneticin (G418, Thermo Fisher Scientific), and cell pools with high and low expression levels of SRSF4–GFP and SRSF6–GFP were sorted by fluorescence-activated cell sorting (FACS) and expanded. Human umbilical vein endothelial cells (HUVECs) were cultured in pre-coated plates [0.1% gelatin–phosphate-buffered saline (PBS), Sigma Aldrich] in endothelial basal media (Lonza, Basel, Switzerland) supplemented with EGM™ Single Quots™ (Lonza, Basel, Switzerland) and 10% (v/v) FBS. HUVECs were cultured in 10 cm dishes until the second passage and subsequently passaged for the experiments.

Hypoxia and inhibitor treatments

For hypoxia treatment, cells were either grown in normoxic conditions (37°C, 21% O_2, 5% CO_2) or incubated and harvested in a hypoxia station (4 h or 24 h, 37°C, 0.2% O_2, 5% CO_2; Hypoxystation H35, Don Whitley ScientificLimited, Oxford Optronix). To stabilize HIF1α, cells were grown until 60% confluency and were then incubated for 24 h with fresh medium containing 250 μM $CoCl_2$ (Sigma Aldrich) or DMSO (dimethylsulfoxide, Sigma Aldrich) as a control. To block nonsense-mediated decay (NMD), cells were treated with 100 μg/ml cycloheximide (CHX, Sigma Aldrich) or DMSO 2 h before harvesting. To inhibit the proteasome, cells were treated with 10 μM MG132 (Sigma Aldrich) or DMSO for 4 h prior to harvesting.

RNA isolation, reverse transcription, RT-PCR and qPCR

Cells were harvested and resuspended in TRIzol (Thermo Fisher Scientific). RNA was extracted according to the manufacturer's instructions, treated with TURBO DNase (Thermo Fisher Scientific) for 30 min at 37°C to remove genomic DNA and subsequently purified. To obtain semi-extractable RNAs, the TRIzol samples were split, and one half was heated for 10 min at 55°C prior to RNA extraction. A 1–2 μg aliquot of RNA was reverse transcribed into cDNA using the Superscript III kit (Life Technologies) with 10 mM dNTP Mix (Thermo Fisher Scientific) and a mixture of oligo $d(T)_{18}$ and random hexamers (Sigma Aldrich). For quantitative polymerase chain reaction (qPCR), primers were selected using Primer-BLAST (https://www.ncbi.nlm.nih.gov/tools/primer-blast/). qPCRs were performed using cDNA (1:8 dilution) and the ORA SEE qPCR Green ROX L kit (highQu) on a PicoReal 96 machine (Thermo Fisher Scientific). For splicing PCRs, primers were designed using SnapGene (San Diego) binding within upstream and downstream exons flanking the regulated cassette exons (CEs). For circRNAs, divergent primers were designed to bind on the left and right of the back-splice junctions. Real-time PCRs (RT-PCRs) were performed using Taq DNA polymerase (New England Biolabs) with an appropriate number of cycles within the exponential phase (generally 28 cycles). RT-PCR products were analyzed either by standard agarose gel electrophoresis, where images were acquired with a ChemiDoc MP Imaging System (Bio-Rad) and quantification of isoform fractions was performed with Fiji from at

least three replicates, or by capillary electrophoresis using the Agilent DNA 1000 Kit on the Agilent Bioanalyzer 2100 System. GraphPad Prism was used for graphics/statistics. All primers used are listed in Supplementary Table S1.

RNA-seq, differential gene expression and splicing analyses

For RNA sequencing (RNA-seq), 5 μg of total RNA were subjected to ribo-depletion and library generation by Novogene (Cambridge). Libraries were either sequenced on an Illumina HiSeq 4000 machine (single-end 75 nt reads, 30 million reads, three replicates per condition) or a NovaSeq 6000 machine (paired-end 150 nt reads, 60 million reads, two replicates per condition). RNA-seq reads were mapped against the human genome (version hg38) with GENCODE gene annotation using STAR (v2.6.1d) (38) with the following parameters:

```
STAR \ --runMode alignReads
--outSAMattributes All
--outSAMtype BAM SortedByCoordinate
--outFilterMismatchNmax 999
--outFilterMultimapNmax 1
--outFilterMismatchNoverLmax 0.04.
```

Reads were counted into exons of genes using htseq-count (39) with default parameters, and the count tables were used as input for differential gene expression analyses with DESeq2 (version 1.22.2) (40). Genes with an adjusted *P*-value <0.01 and an absolute fold change (FC) >1.5-fold were considered significant. Gene Ontology (GO) enrichment analysis was performed with hypeR or with the over-representation test implemented in the enrichGO function of the clusterProfiler package in R (41). Enrichment was tested against the union of all genes that were tested in the DESeq2 analysis. Adjusted *P*-value cut-offs were set to 0.05 and 'biological process' categories were explored.

Splicing analysis was performed using MAJIQ (version 2.2) (42). Specifically, we used the majiq-build function to construct a single splice graph over all replicates and conditions. Next, majiq-deltapsi was used to quantify local splicing variations (LSVs) between control and hypoxic conditions for the HeLa WT and SRSF6 OE datasets. Identified LSVs from both comparisons were considered significantly regulated with an absolute difference in junction usage (percent selected index, PSI) of |ΔPSI| >5% and a changing probability >50%. Non-regulated LSVs were considered with |ΔPSI| <2% and a changing probability of 0%. Both regulated and non-regulated LSVs were subsequently stratified to the binary level. First, we identified the two main junctions per LSV based on the ΔPSI, retaining only those LSVs for which at least 50% of the change seen in the strongest junction can be explained by the second strongest junction. LSVs were classified into the events 'intron-retention', 'alternative 3′ splice site', 'alternative 5′ splice site' and 'cassette exon'. This was done by combining source and target LSV junctions for a given event, requiring both LSVs to be regulated as defined above. CE events were further subclassified into 'simple cassette exon', 'alternative first exon', 'alternative last exon' and 'complex events' using the same methodology. This stratification collapsed 2744 regulated LSVs including simple CEs into 727 binary events of the same category (Figure 1A; Supplementary Figure S1A) with precisely defined start and end coordinates for further analyses. For RNA maps, we additionally identified the upstream and downstream constitutive exons of all simple CEs.

CircRNA analysis

CircRNAs were detected and quantified with the workflow Calcifer (Brezski *et al.*, manuscript in preparation), which combines the output of CIRCexplorer2 (version 2.3.8) (43) and CIRI2 (version 2.0.6) (44). For CIRCexplorer2, RNA-seq reads were mapped against the reference genome (GRCh38.p13, Gencode v39, primary annotation) using STAR (version 2.7.6a) (38) with the following parameters:

```
--outFilterMultimapNmax 1
--outFilterMismatchNmax 2
--alignSJDBoverhangMin 15
--alignSJoverhangMin 15
--chimSegmentMin 15
--chimScoreMin 15
--chimScoreSeparation 10
--chimJunctionOverhangMin 15.
```

The chimeric junctions from STAR were used as input for CIRCexplorer2. For CIRI2, RNA-seq reads were aligned against the same reference genome using BWA (version 0.7.17) (45) with the parameter –T 19 to pre-filter the resulting alignments. CIRCexplorer2 and CIRI2 were run with default parameters, and circRNAs detected by both tools were combined and filtered. CircRNAs that lacked a canonical splice site or were longer than 100 kb were filtered out and supporting reads for each circRNA from the chimeric junctions output were recounted as described before (17). Only circRNAs that had at least two unique mapped reads across the back-splice junction in at least one replicate were kept. The differential abundance of high-confidence circRNAs (≥5 mapped reads) was analyzed with DESeq2 (version 1.30.1) (40) by combining the back-splice read counts of all circRNAs and the linear read counts for all genes into a joint input for DESeq2 (17).

iCLIP library preparation

Cells were grown in triplicate on 14 cm culture dishes in normoxia or hypoxia (4 h and 24 h) until 90% confluency. Cells were irradiated once with 150 mJ/cm^2 UV light at 254 nm (CL-1000, UVP) on ice and immediately harvested in a hypoxia chamber (Hypoxystation H35, Don Whitley ScientificLimited, Oxford Optronix). iCLIP (individual-nucleotide resolution cross-linking and immunoprecipitation) was performed as described in (46) with minor modifications. Briefly, cross-linked RNA was digested into smaller fragments using RNase I (Invitrogen) prior to immunoprecipitation (IP). Dynabeads Protein G (Invitrogen) coupled to goat α-GFP antibodies (MPI-CBG, Dresden, Germany) were used for IP. Purified RNA fragments were ligated to pre-adenylated DNA 3′ adapters (Integrated DNA Technologies) and reverse-transcribed using barcoded reverse transcription primers utilizing Superscript IV (Thermo Fisher Scientific). cDNA fragments were size-selected and circularized by CircLigase II (Epicentre/Lucigene) before

re-linearization using BamHI HF (New England Biolabs). The final libraries were amplified using AccuPrime SuperMix I (Thermo Fisher Scientific) and subjected to Illumina sequencing on a HighSeq2000 instrument with 75 nt single-end reads (20 million reads per replicate).

iCLIP data analysis

iCLIP sequencing data were processed according to (47) with minor changes. In brief, adapter sequences were trimmed from the right end of the reads with a minimum overlap of 1 nt and a minimum error rate of 1% using Flexbar (version 3.0.3). Quality control was performed before and after read trimming using FastQC (version 0.11.5). Trimmed reads were mapped to the human reference genome hg38 with STAR (version 2.5.3a) (38), allowing two mismatches without soft-clipping of the read 5′ ends. Uniquely mapping reads were retained and PCR duplicates were removed with UMI-Tools (version 0.2.1) (48).

Processed reads from three replicates and three conditions were merged prior to peak calling with PureCLIP (version 1.3.1) (49) using a minimum transition probability of 1%. Significant cross-link sites (1 nt) were filtered by their PureCLIP score, removing the lowest 2% of cross-link sites. The remaining sites were merged into 7 nt wide binding sites using the R/Bioconductor package BindingSiteFinder (version 1.0.0), filtering for sites with at least three positions covered by cross-link events. All binding sites were controlled for reproducibility across conditions by requiring support from two out of three replicates. A replicate supported a binding site when it harbored more cross-links than the replicate-specific threshold, defined by the 10% quantile of the distribution of cross-links in all binding sites (47).

Binding sites were overlapped with gene and transcript annotations obtained from GENCODE (release 29). Binding sites within protein-coding genes were assigned to the transcript regions, i.e. intron, coding sequence (CDS), 3′-untranslated region (3′UTR) or 5′UTR. The assignment was based on a majority vote for multiple overlapping annotations, followed by the hierarchy CDS >3′UTR >5′UTR >intron to resolve ties.

Local sequence content around SRSF6-binding sites was assessed separately for CDS and introns by counting hexamer frequencies in a 101 nt window centered at the binding sites. Frequencies were normalized by the respective set size. The 10 most enriched hexamers were aligned with ClustalW and sequence logos were computed from the resulting position–weight matrix using the R/Bioconductor packages msa and ggseqlogo (50,51).

RNA maps were computed by counting cross-link events mapping to simple CE events. The 5′ and 3′ splice sites of the CEs as well as 5′ splice sites of the upstream and 3′ splice sites of the downstream exons were used as reference points to span a 100 nt window. For RNA maps on all identified CEs (regulated and non-regulated), cross-link events were summarized per iCLIP condition and normalized to the library size (see Figure 6D). For RNA maps on regulated exons (more or less included), cross-link events were summarized over all conditions and normalized to the set size (Supplementary Figure S6E, F). The iCLIP signal was represented as normalized cross-link events with a local polynomial regression fitting (loess) over this signal.

TCGA correlation analyses

Gene and junction read counts were retrieved for samples of the BRCA (breast invasive carcinoma), CESC (cervical squamous cell carcinoma and endocervical adenocarcinoma), COAD (colon adenocarcinoma), KICH (kidney chromophobe). LIHC (liver hepatocellular carcinoma) and STAD (stomach adenocarcinoma) cohorts via the create_rse (type = 'gene'/'jxn') and transform_counts (only for gene read counts) function of the R/Bioconductor package recount3 (52) which creates a RangedSummarizedExperiment object containing the necessary counts and additional meta information (e.g. sample type or batch identifier). Samples were restricted to those labeled as 'Primary Tumor' (tumor) or 'Solid Tissue Normal' (normal) and, in the case of the BRCA cohort, to samples from female participants. For gene expression quantification, the gene read counts were normalized and transformed via the estimateSizeFactors and vst function of the R/Bioconductor package DESeq2 (40). In addition, the vst-transformed counts were batch-corrected via the removeBatchEffect function of the R/Bioconductor package limma, using the batch identifiers provided by the recount3 package. For the calculation of *SRSF6* poison cassette exon (PCE) inclusion levels, counts of the two inclusion junctions and of the skipping junction of the PCE were extracted for all samples, followed by the calculation of PSI values by dividing the mean of the two inclusion junctions by that value plus the counts of the skipping junction. PSI values were only calculated for samples where the three junctions comprised at least 25 reads. Hypoxia scores for tumor samples of the BRCA, CESC and LIHC cohort were extracted from (53) and correspond to the Buffa signature. BRCA subtype classification was downloaded from the GDC and is based on the PAM50 signature established by The Cancer Genome Atlas (TCGA) Network (54).

SRSF6 knockdown

SRSF6 knockdown (KD) was performed in WT cells in normoxic conditions. HeLa cells were transfected with a pool of two small interfering RNAs (siRNAs; Sigma Aldrich), targeting two different sequences within the *SRSF6* transcript, at a final concentration of 66 nM using jetPRIME Transfection Reagent (Polyplus). The mission universal negative control siRNA (Sigma Aldrich) was used as control. After 48 h, cells were harvested for RNA and protein extraction. The siRNAs are listed in Supplementary Table S2.

PCE 3′ splice site deletion by CRISPR/Cas9 genome editing

To delete the 3′ splice site of the *SRSF6* PCE, two single guide RNAs (sgRNAs) were designed using CRISPOR (http://crispor.tefor.net) and purchased from IDT (Integrated DNA Technologies). Purified sgRNAs were preassembled with recombinant clustered regularly interspaced short palindromic repeats (CRISPR)-associated protein 9 (Cas9) (IDT, Alt-R HiFi Cas9 Nuclease). HeLa WT cells were transfected with the ribonucleoproteins (RNPs) using Lipofectamine CRISPRMAX (Invitrogen) and cultured for 48 h in the presence of an HDR enhancer (20 μM, IDT). CRISPR clones were generated by limited

dilution and grown from single cells in 96-well plates. For genomic screening, cells were washed twice with PBS in the 96-well plates and lysed in directPCR buffer (20 mM Tris–HCl, pH 8, 200 mM NaCl, 1 mM EDTA, 0.5% Tween-20, 0.5% NP-40) with freshly added 200 μg/ml proteinase K (Sigma Aldrich), and incubated for 1 h at 55°C followed by proteinase K inactivation at 95°C for 15 min. Screening PCRs were performed from crude lysates using primers flanking the PCE region. The primers are listed in Supplementary Table S1 and sequences of the gRNAs in Supplementary Table S2.

Western blot and antibodies

Cells were lysed in 300 μl of NET-2 buffer (150 mM NaCl, 0.05% NP-40, 50 mM Tris, pH 7.5), supplemented with cOmplete Protease Inhibitor Cocktail (Sigma Aldrich) and 10 mM β-glycerophosphate (Fluka BioChemica). Lysates were sonicated on ice for 30 s (three pulses of 10 s; 20 s intervals) at 20% amplitude (Branson W-450 D) and cleared by centrifugation. Protein concentrations were measured using Quick Start Bradford 1× Dye Reagent (Bio-Rad) on a NanoDrop2000 (Thermo Fisher Scientific). A 20–30 μg aliquot of protein was separated by sodium dodecylsulfate (SDS)–polyacrylamide gel electrophoresis (PAGE) either on 8% stain-free gels (Bio-Rad) or on NuPAGE 4–12% Bis-Tris gels (Thermo Fisher Scientific) and transferred onto nylon membranes (0.1 μm pore size, EMD Millipore). Transfer and equal loading were evaluated by activation of stain-free gels by UV light. Membranes were probed with the following antibodies and dilutions in Tris-buffered saline/Tween (TBST): 1:3 α-mouse mAb104 (CRL_2067; ATCC), 1:100 α-rabbit HIF1α (NB100-134; Novus Biologicals), 1:100 α-rabbit SRSF6 (LS-C29032711; LifeSpan Biosciences), 1:1000 α-rabbit SRSF4 (NBP2-04144, Novus Biologicals), α-mouse BNIP3 (ab10433, Abcam) and α-rabbit alpha-tubulin antibody (ab176560; Abcam). Image acquisition and quantification were performed using the ImageLab software (Bio-Rad).

SRSF6–GFP immunoprecipitation and mass spectrometry (MS) analysis

Cells were grown in two replicates on 14 cm culture dishes in normoxia or 24 h hypoxia and harvested in a HypoxyLab station (Oxford Optronix, UK). For stringent IPs, 100 μl of beads (Dynabeads Protein G, Thermo Fisher Scientific) were washed and resuspended in 200 μl of lysis buffer (100 mM NaCl, 1% NP-40, 0.1% SDS, 0.5% sodium deoxycholate, 50 mM Tris, pH 7.4) and incubated with 12 μg of goat IgG α-GFP antibodies (MPI-CBG, Dresden, Germany) on a rotating wheel at 4°C for 1 h. Goat IgG (Sigma) served as the specificity control. Beads were washed with high-salt buffer (1 M NaCl, 1% NP-40, 0.1% SDS, 0.5% sodium deoxycholate, 1 mM EDTA, 50 mM Tris, pH 7.4) and lysis buffer. Cells were lysed in ice-cold lysis buffer supplemented with cOmplete Protease Inhibitor Cocktail (Sigma) and 10 mM β-glycerophosphate (Fluka BioChemica), and sonicated (see above). Lysates were treated with TURBO DNase (Thermo Fisher Scientific) for 5 min at 37°C and were cleared by centrifugation (17 000 *g*, 10 min, 4°C). Beads were incubated with the cell lysates at 4°C for 1.5 h on a rotating wheel, washed with high-salt buffer and lysis buffer without detergents and snap-frozen for subsequent MS analysis. The beads were digested with trypsin and LysC overnight and the eluted proteins were analyzed by liquid chromatography/MS (LC/MS).

Analysis of MS data

LC/MS was performed on a Thermo Scientific™ Q Exactive Plus equipped with an ultra-high performance liquid chromatography (UHPLC) unit (Thermo Scientific Dionex Ultimate 3000) and a Nanospray Flex Ion-Source (Thermo Fisher Scientific). Peptides were separated on a column with a 2.4 μm Reprosil C18 resin (Dr. Maisch GmbH) in-house packed picotip emitter tip (diameter 100 μm, 15 cm from New Objectives) with a gradient from 4% acetonitrile, 0.1% formic acid to 60% eluent B (99% acetonitrile, 0.1% formic acid) in two steps for 35 min. MS data were recorded by data-dependent acquisition. Peptides and proteins were identified and quantified using PEAKS 7 Studio (Bioinformatics Solutions Inc. Waterloo, Canada), human reference proteome set (UniProt, May 2020, 74 823 entries, supplemented with SRSF6–GFP) with a false discovery rate (FDR) <1%. Oxidation of methionine (+15.99), deamidation on asparagine and glutamine (+0.98), phosphorylation on serine, threonine and tyrosine (+79.97) and carbamidomethylation (+57.02) on cysteine were selected as variable.

5-Ethynyl-2'-deoxyuridine (EdU) proliferation assay and doubling times

Proliferation of HeLa cells was measured using the Click-iT® EdU Imaging Kit (Invitrogen) following the manufacturer's instructions, with minor modifications. Briefly, cells from subconfluent cultures were seeded onto 12 mm coverslips placed into 24-well plates and incubated for 24 h under either normoxic or hypoxic conditions. After 18 h of incubation, 250 μl of medium was removed and 250 μl of fresh DMEM containing 20 μM EdU was added to each well and mixed to a final concentration of 10 μM. After 6 h of incubation with EdU, the medium was discarded, cells were washed with PBS and fixed with 4% paraformaldehyde (PFA) in PBS for 15 min. Cells were washed with 3% bovine serum albumin (BSA) in PBS, permeabilized with 0.5% Triton X-100 in PBS for 20 min and washed again with 3% BSA in PBS. Fixed cells were then incubated with the Click-iT reaction cocktail containing Alexa Fluor® 647 azide (diluted 4× in H_2O) for 30 min and washed with 3% BSA in PBS. DNA was stained with Hoechst 33342 (5 μg/ml, Sigma Aldrich) for 30 min and then the coverslips were washed with PBS, dried briefly and mounted onto glass slides using ProLong Diamond Antifade Mountant (Invitrogen).

For the estimation of the doubling times, cells were harvested at different time points by trypsinization, mixed 1:1 with Trypan Blue Solution (0.4%, Gibco) and live cells were counted using an automated cell counter (EVE Automated Cell Counter, NanoEnTek). Growth curves were plotted using GraphPad Prism (https://www.graphpad.com), and

doubling times were calculated after applying the exponential growth fit (Mathusian) of logarithmic cell populations.

RNA fluorescence *in situ* hybridization and immunofluorescence (FISH-IF)

For FISH-IF experiments, 12 mm coverslips were placed inside 10 cm plates used for the experiments. After removing the medium and washing the cells with 1× PBS, the coverslips were transferred to 24-well plates. Cells were fixed with 4% PFA in PBS for 15 min, washed with PBS and permeabilized with 70% ethanol for 1 h. FISH was performed using Stellaris probes and buffers (LG Biosearch Technologies) following the manufacturer's protocol. Coverslips were washed with Stellaris Wash Buffer A, placed in a humidified chamber and hybridized for 16 h at 37°C in the dark with *MALAT1* probes (human *MALAT1* with Quasar 670 Dye, BioCat) and mouse SC35 antibody (Abcam) as nuclear speckle (NS) markers both diluted 1:100 in Stellaris Hybridization Buffer. To visualize DNA damage, mouse α-H2A.X PhosphoSer139 antibody (BioLegend) was used as a marker at 2 μg/ml final concentration. After hybridization, the coverslips were incubated with Stellaris Wash Buffer A containing the secondary antibody (donkey α-mouse coupled to Alexa Fluor 555, Abcam) in a 1:500 dilution for 30 min at 37°C. DNA was stained with Hoechst 33342 (Sigma Aldrich) at a final concentration of 5 μg/ml in Wash Buffer A for 30 min at 37°C and then the coverslips were washed with Wash Buffer B, dried for 15 min and mounted onto glass slides using ProLong Diamond Antifade Mountant (Invitrogen).

Image acquisition and quantification

Images were acquired with a confocal laser-scanning microscope (LSM780; ZEISS) or a Zeiss Cell Observer SD spinning disc microscope, with a Plan-Apochromat 63× 1.4 NA oil differential interference contrast objective using the Zen 2012 (black edition; 8.0.5.273; ZEISS). Fluorescence signal was detected with an Argon laser (GFP 488 nm, Qasar 570–561 nm and Qasar 670–647 nm). Images from the same experiment were acquired on the same day with the same settings for all conditions. Line scans were performed by drawing a straight line across the nucleus, without crossing the nucleolus. Fluorescence intensity per pixel in the line area was acquired using the 'Plot Profile' tool. Images were analyzed using Fiji (55). Pictures were cropped with the Image crop function and scale bars were added. EdU-stained images were analyzed as follows: for each cell line in each condition, at least 39 images from two independent biological replicates, each containing between 21 and 59 cells, were analyzed, for a total of at least 1199 cells per cell line per condition. For each picture, the number of nuclei (Hoechst staining) and the number of EdU-positive nuclei were counted and the percentage of EdU-positive nuclei was calculated. For fluorescence quantification, the Hoechst channel was used to acquire a threshold image ('Threshold Li') and the 'Particle analyzer' plug-in from the Biovoxxel toolbox (https://imagej.net/BioVoxxel_Toolbox) was used to obtain the nuclear regions of interest (ROIs). ROIs were transferred to the GFP channel and fluorescence was quantified using the 'integrated density value' (mean gray value per pixel × area). To count micronuclei, random pictures were taken until 50–150 cells were imaged in 3–5 biological replicates, and the number of micronuclei per 100 cells was calculated for each replicate. Data were plotted using GraphPad Prism 8 (https://www.graphpad.com), and cell lines and conditions were compared using a two-tailed unpaired Student's *t*-test.

Statistical analyses of qPCRs and Western blots

For the visualization and statistical testing of qPCR quantifications, C_T values of the gene of interest were normalized to the C_T value of a housekeeping gene (*U6* or 18S RNA) resulting in ΔC_T (dCT) values. Next, the mean dCT value for a reference group was computed (typically Nor or WT-Nor) and all dCT values were normalized to the mean ΔCT value of the reference group, resulting in ΔΔCT (ddCT) values (corresponding to a $\log_2$-transformed FC of a given condition over the reference group). Figures show individual ddCT data points together with the mean and standard deviation (SD) of ddCT values per group.

For the visualization and statistical testing of western blot quantifications, the mean normalized intensity for a reference group was computed (Nor). Next, all normalized intensities were normalized to the normalized intensity of the reference group, leading to 'relative protein levels' (corresponds to an FC). Figures show individual data points together with the mean and SD of the relative protein level per group.

Statistical tests were performed on the ddCT values (qPCR) and relative protein levels (western blots). For comparisons of more than two conditions (e.g. normoxia and hypoxia in WT and SRSF6 OE cells), a one-way analysis of variance (ANOVA) with a Tukey's honestly significant difference (HSD) post-hoc test was performed. For comparisons including only two conditions, a two-sample Student's *t*-test was performed.

RESULTS

HeLa cells adapt to hypoxia through global exon skipping

To better understand the mechanisms of AS-mediated adaptation in response to acute hypoxia (24 h; 0.2% O_2), we performed RNA-seq in HeLa cells and analyzed changes in AS using MAJIQ (42). We found 7178 LSVs that changed significantly after 24 h of hypoxia [absolute difference in junction usage (|ΔPSI|) >5%; Figure 1A]. The majority of LSVs affected alternative CEs (4238, 59%), which more often showed increased skipping (62%) (Figure 1B; Supplementary Figure S1A, B). Generally, skipped exons were significantly shorter than those that were more included (Figure 1C). Semi-quantitative RT-PCR experiments validated nine out of nine splicing events, comprising seven exon skipping and two exon inclusion events (Figure 1D, E, $n = 3$; *P*-value <0.05).

To identify putative regulators of the widespread AS changes in hypoxia, we used DESeq2 to quantify differential gene expression (40). We found 7195 protein-coding and 1298 non-coding genes differentially expressed in hypoxia [FDR <0.05, absolute FC (|FC|) >1.5]. While mR-

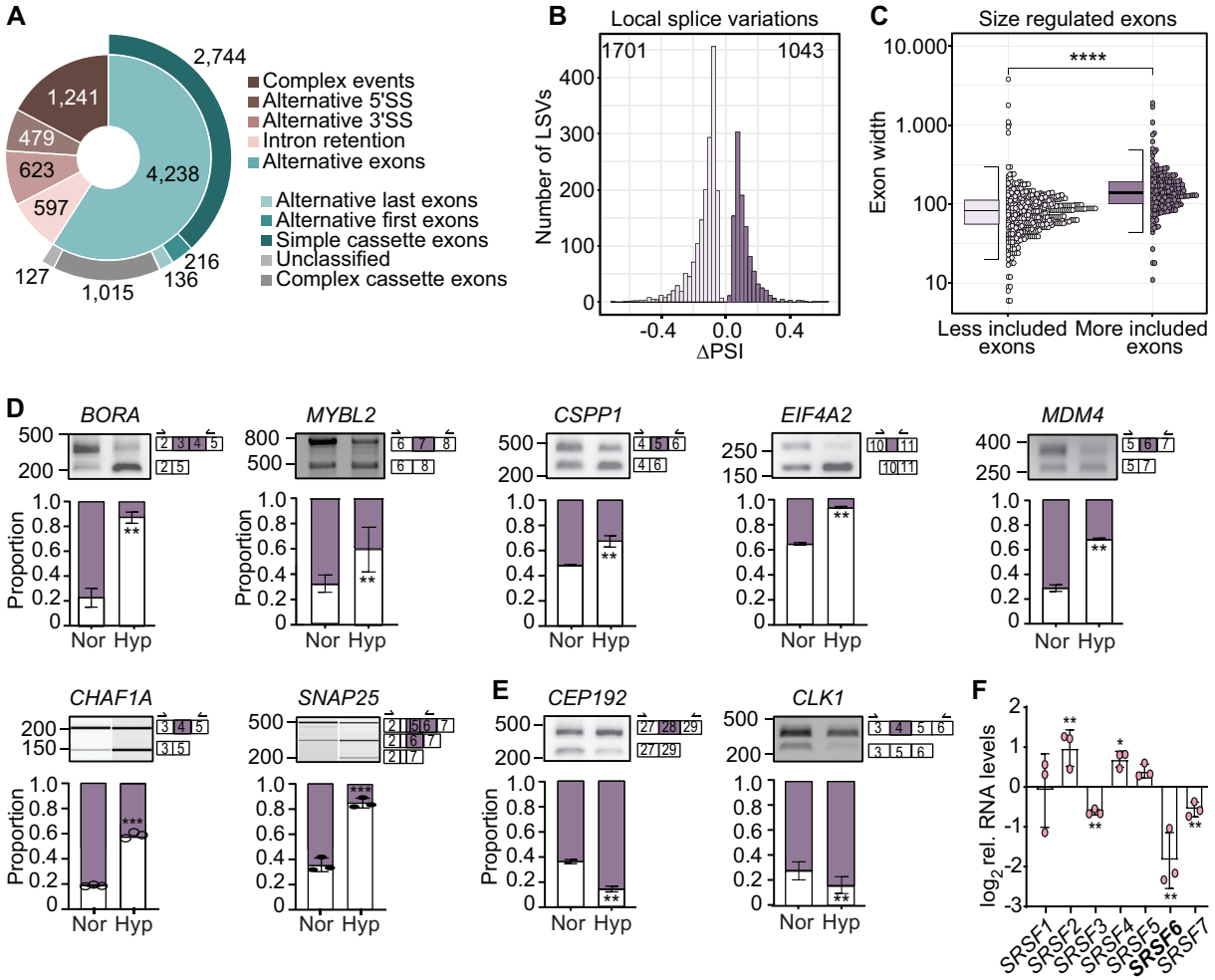

Figure 1. HeLa cells adapt to hypoxia through global exon skipping. (**A**) Pie chart displaying the total number of significantly changing LSVs in hypoxic (0.2% O_2) compared with normoxic (21% O_2) HeLa WT cells separated into distinct splice events; $n = 3$ replicates per condition. (**B**) Histogram showing the difference in inclusion junction usage (ΔPSI) of regulated simple CEs in hypoxic WT cells. Numbers of more or less included exons are shown. (**C**) Bee swarm plot comparing the distribution of exon length of simple CEs for less and more included exons. Wilcoxon rank sum test: ****P-value <2.2e-16. (**D** and **E**) Semi-quantitative RT-PCR splicing gels validating seven CEs that were less included (D) and two CEs that were more included (E) under hypoxia. Alternative CEs are marked in purple. Black arrows above the exons indicate the primer positions. Size markers (in bp) are shown on the left side of each gel picture. Relative proportions of exon-including isoforms, shown in purple, quantified from three independent experiments. (**F**) RT–qPCR validation of changes in SR protein transcript levels (*SRSF1-7*) after 24 h hypoxia ($n = 3$). *U6* snRNA transcript levels were used for normalization. All data: Student's t-test: *P-value <0.05, **P-value <0.01.

NAs showed roughly equal amounts of up- and down-regulation, non-coding RNAs (ncRNAs) tended to be more often up-regulated in hypoxia (Supplementary Figure S1C). Up-regulated genes were enriched in biological processes such as 'angiogenesis' and 'negative regulation of cell proliferation', while down-regulated genes were involved in mitochondrial gene expression, translation and RNA processing (Supplementary Figure S1D). In line with global changes in splicing, 'RNA splicing' was among the most down-regulated biological processes. This was reflected in reduced levels of several SR proteins (SRSF1, SRSF3, SRSF6, SRSF7 and SRSF8), while heterogeneous ribonuclear proteins (hnRNPs) remained mostly unchanged (Supplementary Figure S1E). Quantitative reverse transcription–PCR (RT–qPCR) confirmed that *SRSF3*, *SRSF6* and *SRSF7* levels decreased significantly upon hypoxia, whereas *SRSF2* and *SRSF4* were increased (Figure 1F). Together, these data show that hypoxia decreases the expression of specific splicing factors and causes global exon skipping.

SRSF6 levels and splicing activity are strongly reduced under acute hypoxia

SRSF6 showed the strongest decrease in transcript levels among all SR protein family members tested (~4-fold), suggesting that low SRSF6 levels might be partly responsible for the widespread exon skipping in hypoxia. Indeed, the consensus binding motif of SRSF6 (GAAGAA) (56,57) was enriched in hypoxia-skipped exons, while the binding motif of SRSF1 (GGA) (58) was enriched in exons that were more included (Figure 2A). In agreement with the down-regulation of *SRSF6* mRNA levels, SRSF6 protein levels were reduced by 60% after 24 h hypoxia; at the same time, the relative levels of phosphorylated SRSF6 significantly in-

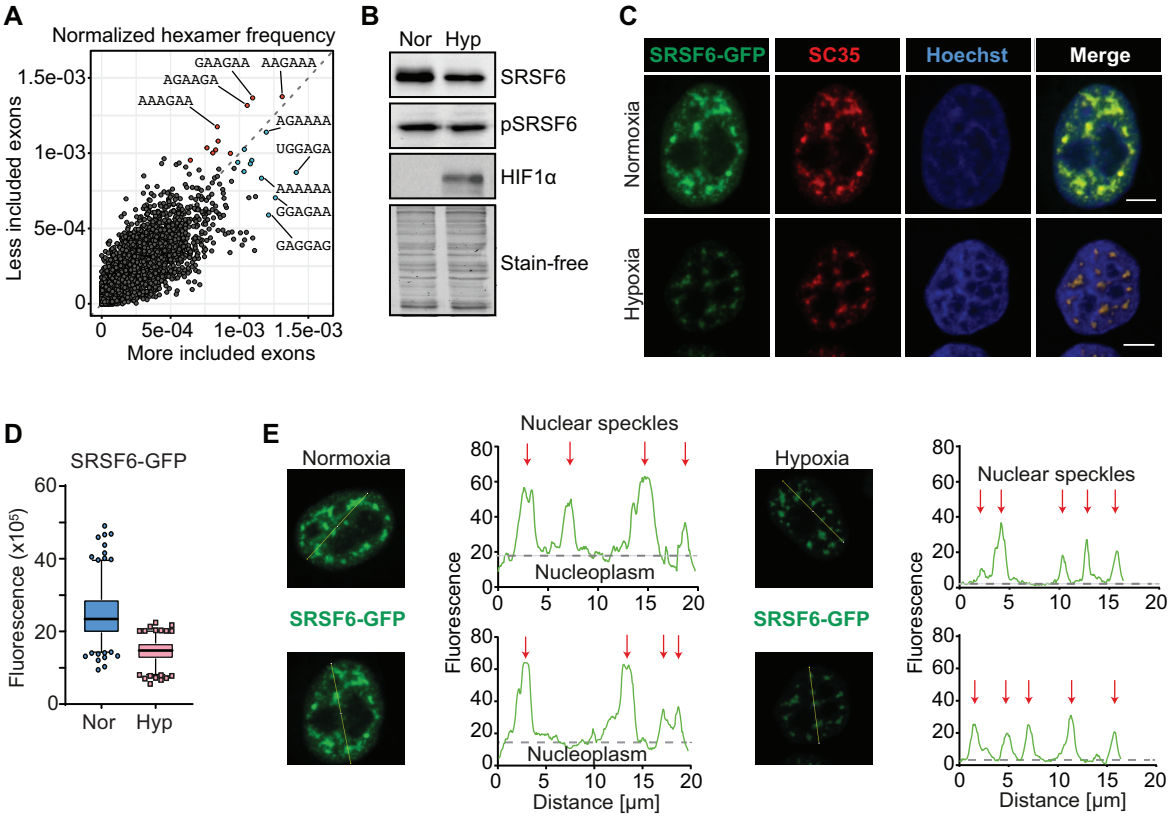

Figure 2. SRSF6 levels and splicing activity are strongly reduced under acute hypoxia. (**A**) Scatter plot comparing hexamer frequencies in exons that are more or less included after 24 h hypoxia. (**B**) Representative western blot showing that total SRSF6 protein levels but not those of phosphorylated SRSF6 (pSRSF6) decrease in hypoxia. pSRSF6 was detected using mAb104 antibody. HIF1α was used as hypoxia control, and a stain-free gel is shown as loading control. (**C**) Representative confocal fluorescence microscopy images showing the distribution and levels of SRSF6–GFP in normoxic and hypoxic HeLa cells. SRSF6–GFP signal (green), NSs labeled with α-SC35 (red), nuclear staining with Hoechst (blue) and the merge of all channels are shown. Scale bars = 5 μm. (**D**) Quantification of SRSF6–GFP fluorescence intensity in normoxia and hypoxia using Fiji ($n > 100$ cells, two replicates). (**E**) Line scan profiles from SRSF6–GFP cells in normoxia and hypoxia. Left: corresponding lines are shown in the micrographs. Right: plots with signal intensity per pixel and line distance. Red arrows indicate GFP peaks with NS localization.

creased (pSRSF6; Figure 2B; Supplementary Figure S2A, B). This indicates that the remaining SRSF6 protein is proportionally more phosphorylated under hypoxia, as suggested for other SR proteins (29).

To study the effect of hypoxia on the subcellular localization of SRSF6, we generated a HeLa cell line stably expressing GFP-tagged SRSF6 at low levels (SRSF6–GFP) through insertion of a BAC containing the complete *SRSF6* gene in the genome (59) (Supplementary Figure S2C). Mirroring the endogenous SRSF6 protein, SRSF6–GFP was also down-regulated in hypoxia (Figures 2C, D and 6A). MS analysis of SRSF6–GFP purified from normoxic and hypoxic cells confirmed that peptides from its RS domain were more often phosphorylated in hypoxia (1.2 versus 0.70 phospho sites/peptide; Supplementary Figure S2D, E). Residual SRSF6–GFP was exclusively detectable in NSs, where phosphorylated SR proteins are normally stored in their inactive form (60) (Figure 2E). These data suggest that the splicing functions of SRSF6 are impaired under hypoxia through a combination of reduced transcript and protein levels and enhanced phosphorylation, which, based on recent studies, is expected to promote skipping of SRSF6 target exons (36,56).

Reduction of SRSF6 levels in hypoxia requires the inclusion of a poison cassette exon

Increased SRSF6 expression in different cancer types is associated with poor prognosis (31,32,34). Thus, understanding the mechanisms by which SRSF6 activity is modulated in hypoxic conditions could be of therapeutic interest. To test whether SRSF6 levels are regulated at the transcriptional level, we treated HeLa cells with $CoCl_2$, which stabilizes HIF1α and HIF2α and thereby mimics the hypoxic transcriptional response (61). $CoCl_2$ treatment for 24 h did not change *SRSF6* transcript, protein or phosphorylation levels (Supplementary Figure S3A–D), suggesting that *SRSF6* transcript levels are not reduced by transcriptional outcompetition by HIF1α or HIF2α (62). SRSF6 reduction was also not rescued by inhibiting the proteasome (Supplementary Figure S3E), excluding a down-regulation of SRSF6 levels via enhanced protein degradation.

MAJIQ analyses indicated that exon 3 of *SRSF6* was ∼3-fold more included in hypoxia (Figure 3A, B). SRSF3, which was similarly down-regulated in hypoxia, also showed more inclusion of exon 4 (Supplementary Figure S3F). Both exons are so-called PCEs that contain premature termination codons (PTCs). PTC-containing tran-

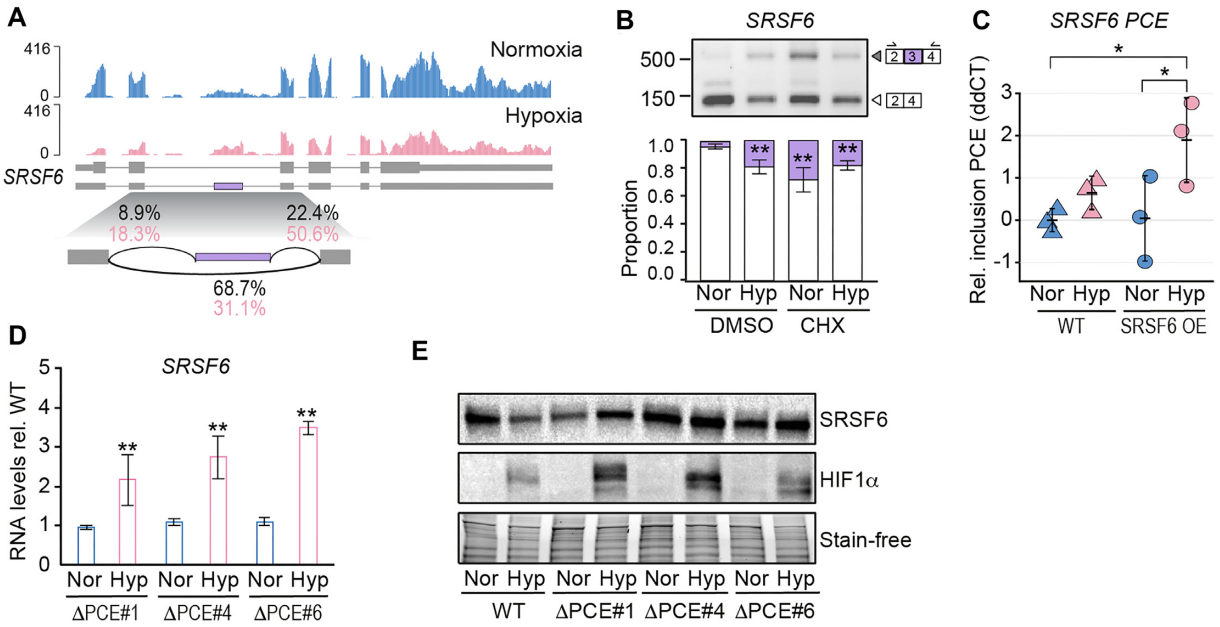

Figure 3. Reduction of SRSF6 levels in hypoxia requires the inclusion of a PCE. (**A**) Sashimi plot showing the distribution of RNA-seq reads on the *SRSF6* gene from HeLa cells cultured under normoxia and hypoxia (24 h). Splice junction read counts are given as a percentage of the total junction read counts. (**B**) Semi-quantitative RT-PCR splicing gels comparing the inclusion of *SRSF6* exon 3 (PCE) in normoxia and hypoxia, and after CHX treatment. Exon 3 is marked in purple. Black arrows above the exons indicate the primer positions. Relative proportions of the PCE-included isoform, shown in purple, were quantified from $n = 3$ experiments. (**C**) RT–qPCR quantifying *SRSF6-PCE* inclusion in WT and SRSF6 OE cells in normoxia and hypoxia relative to WT cells in normoxia. (**D**) RT–qPCR comparing the levels of *SRSF6* mRNA in hypoxia in WT and three SRSF6ΔPCE clones; $n = 3$. Levels are shown relative to WT cells in the same condition. *U6* RNA was used as housekeeping gene. (**E**) Western blot comparing the levels of total SRSF6 protein in hypoxia in WT and three SRSF6ΔPCE clones. HIF1α was used as hypoxia control, and stain-free membrane images were used as loading controls.

scripts are usually degraded rapidly by NMD (63). Accordingly, in normoxic cells, the levels of both *SRSF6-PCE* and *SRSF3-PCE* isoforms strongly increased after CHX treatment, which inhibits NMD (Figure 3B; Supplementary Figure S3G). In contrast, both *PCE* isoforms were already detectable in hypoxia, and NMD inhibition had no further stabilizing effect (Figure 3B; Supplementary Figure S3G). This suggests that NMD is impaired in hypoxia as proposed in earlier reports (64), and that the *PCE* isoforms are not degraded via this route. Nonetheless, their increased production reduces the levels of the translatable *SRSF6* isoforms. $CoCl_2$ treatment (24 h) did not induce *PCE* isoforms and here SRSF6 mRNA and protein levels remained constant (Supplementary Figure S3B, D, H).

To test whether PCE inclusion causes SRSF6 reduction in hypoxia, we removed the 3′ splice site of the intron immediately upstream of the PCE from the genomic locus of *SRSF6* by CRISPR/Cas9 genome editing (SRSF6ΔPCE; Supplementary Figure S3I). Successful editing was validated by PCR and sequencing (Supplementary Figure S3J). RT–qPCR confirmed that *SRSF6* was no longer downregulated in hypoxia in three homozygous SRSF6ΔPCE clones, all showing 2- to 3-fold higher *SRSF6* transcript levels than WT cells in hypoxia (Figure 3D). The PCE was no longer included in the SRSF6ΔPCE clones in hypoxia (Supplementary Figure S3K) and, importantly, SRSF6 protein levels were not reduced (Figure 3E). Altogether, these data argue that SRSF6 reduction in hypoxia requires inclusion of the PCE.

SRSF4 regulates *SRSF6* levels through PCE inclusion

PCE inclusion is usually promoted by the binding of SR proteins 30–60 nt downstream of the 3′ splice site (65,66). iCLIP data comparing seven SR proteins in normoxia (56,57) showed that after SRSF6, SRSF4 was the second most prominent binder to the *SRSF6* PCE (Figure 4A). This suggests that SRSF6 and SRSF4 might both regulate PCE inclusion and SRSF6 reduction in hypoxia. To test this, we generated and sorted HeLa cells for SRSF4–GFP and SRSF6–GFP overexpression (SRSF4 OE, ∼2-fold; SRSF6 OE, ∼4-fold; Figure 4B). Although SRSF6–GFP levels were reduced to a similar extent to endogenous SRSF6 in hypoxia, SRSF6 OE cells still expressed ∼3 times more SRSF6 protein than WT cells in hypoxia (Supplementary Figure S4A).

SRSF6 and SRSF4 OE both reduced endogenous SRSF6 protein levels in normoxia (Figure 4B), which were further reduced in hypoxia and accompanied by an increase in PCE inclusion (Figure 3C, 4C). Together with the iCLIP data, this suggests that in addition to SRSF6 autoregulation, increased SRSF4 levels in hypoxia (Figure 1F) directly downregulate SRSF6 levels via inclusion of the *SRSF6* PCE.

To assess whether this mechanism might also exist in tumors, we analyzed *SRSF4* and *SRSF6* expression levels as well as PCE inclusion in tumor samples from six TCGA (The Cancer Genome Atlas) cohorts. Of note, *SRSF4* and *SRSF6* levels were significantly anti-correlated in BRCA, COAD and STAD (Figure 4D, top). Moreover, *SRSF4* levels positively correlated with PCE inclusion in all cancer

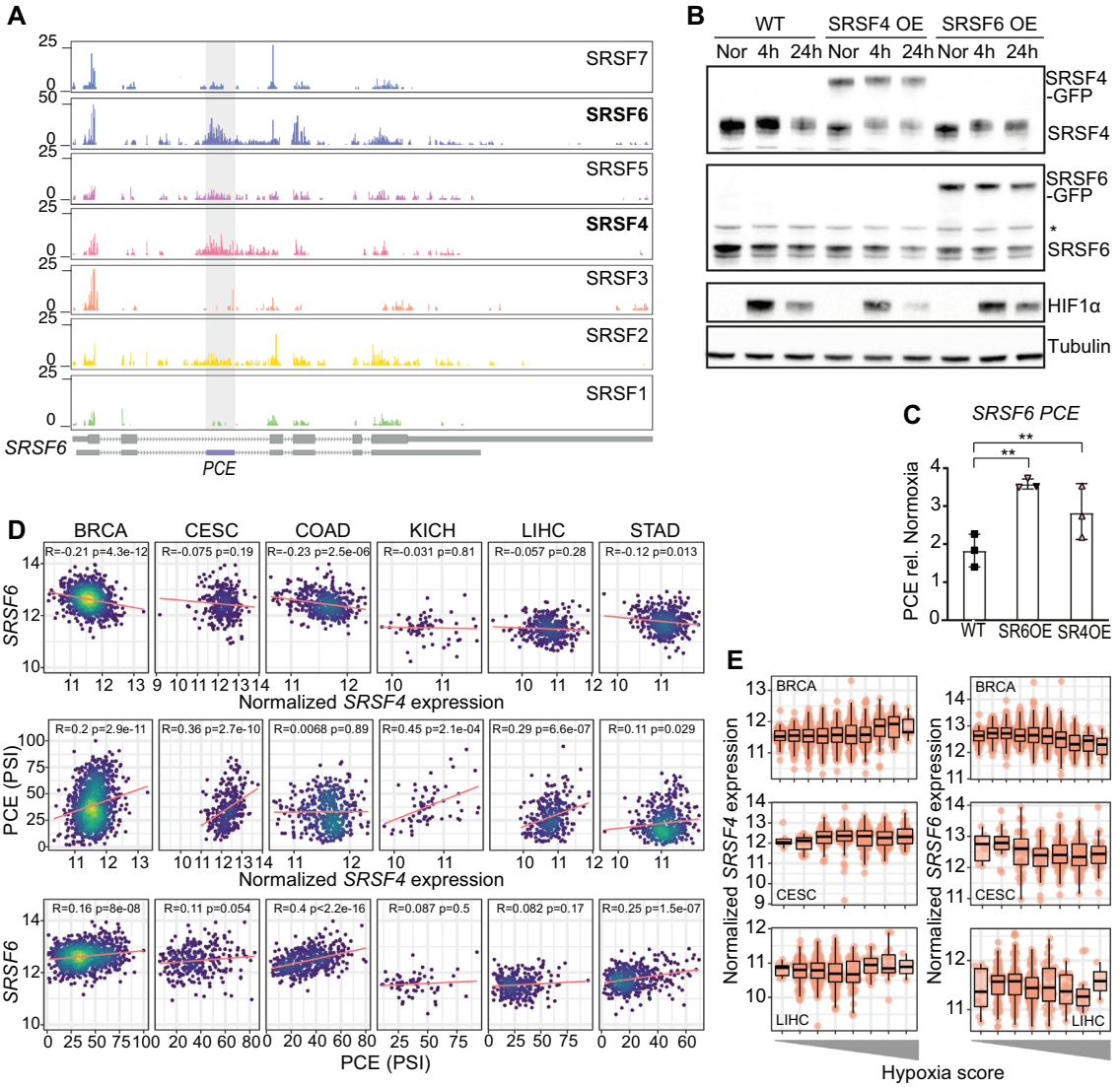

Figure 4. SRSF4 regulates *SRSF6* levels through PCE inclusion. (**A**) Genome browser shot showing normalized cross-link distribution of seven SR proteins on the *SRSF6* gene taken from (57). The PCE is labeled in violet and highlighted in gray. (**B**) Representative western blot of WT, SRSF4 OE and SRSF6 OE cell lines grown in normoxia or hypoxia (4 h and 24 h). Total SRSF4 and SRSF6 protein levels were detected using α-SRSF4 and α-SRSF6 antibodies. The asterisk indicates an unspecific signal. HIF1α is shown as a control for successful hypoxia treatment. Tubulin was used as loading control. (**C**) RT–qPCR quantifying *SRSF6-PCE* inclusion in WT, SRSF6 OE and SRSF4 OE cells in hypoxia relative to normoxia. (**D**) Pairwise correlations of normalized *SRSF4* expression, *SRSF6* expression and *SRSF6-PCE* inclusion levels for tumor samples from six TCGA cancer cohorts. BRCA, breast invasive carcinoma; CESC, cervical squamous cell carcinoma and endocervical adenocarcinoma; COAD, colon adenocarcinoma; KICH, kidney chromophobe; LIHC, liver hepatocellular carcinoma; STAD, stomach adenocarcinoma. (**E**) *SRSF4* and *SRSF6* expression levels in BRCA, CESC and LIHC tumor samples binned by increasing hypoxia score.

types except COAD (Figure 4D, middle row). As controls, we analyzed *SRSF2* and *SRSF5*, which also bind to the *SRSF6* PCE, but less frequently (Figure 4A). *SRSF2* levels correlated positively only in LIHC and *SRSF5* levels only in BRCA and CESC (Supplementary Figure S4B). Incorporation of published hypoxia scores (53) for BRCA, CESC and LIHC tumor samples confirmed that *SRSF4* levels positively correlated with high hypoxia scores while *SRSF6* levels negatively correlated (Figure 4E; Supplementary Figure S4C). Moreover, when BRCA tumor samples were separated by subtype, the most severe basal subtype, which was most hypoxic, was associated with the lowest *SRSF6* but highest *SRSF4* levels (Supplementary Figure S4D, E). Altogether, these data suggest that high SRSF4 levels in hypoxic cancer types may also reduce *SRSF6* levels via PCE inclusion.

Maintaining high SRSF6 levels in hypoxia impairs exon skipping

To test whether reduced SRSF6 levels are important for hypoxia adaptation, we investigated the impact of continued SRSF6 overexpression. We performed RNA-seq and MAJIQ analyses from SRSF6 OE cells to determine the splicing changes between normoxia and 24 h hypoxia. In general, SRSF6 OE cells exhibited more splicing changes com-

pared with the WT in hypoxia (9622 versus 7178 significantly changing LSVs, Figures 1A and 5A), and the proportion of regulated CEs was even higher than in WT cells (68% versus 59%). However, the fraction of skipped exons in hypoxia among regulated CEs was clearly reduced in SRSF6 OE cells compared with WT cells (53% versus 62%), suggesting that exon skipping might be impaired (Figures 1B and 5B). Indeed, of 1701 down-regulated LSVs identified in WT cells, 1150 were not regulated in SRSF6 OE cells (71.3%) and 62 were even up-regulated (Figure 5C–E; Supplementary Figure S5A). Moreover, of 3044 unregulated LSVs in WT cells, 1526 were more included (50.1%) in SRSF6 OE.

SRSF6 OE also impaired the formation of circRNAs in hypoxia, which is usually promoted by low levels of splicing factors and exon skipping (67,68). Our new circRNA pipeline Calcifer (Brezski *et al.*, manuscript in preparation) identified 2428 circRNAs in WT HeLa cells, of which 31 were significantly up-regulated in hypoxia (Supplementary Figure S5B). Strikingly, in SRSF6 OE cells, only 23 of the 2428 circRNAs could still be detected (among a total of only 138 detected circRNAs in SRSF6 OE cells) and none of them was up-regulated in hypoxia (Supplementary Figure S5B), suggesting that SRSF6 OE suppresses back-splicing. In line with this, of 13 circRNAs that we had validated as circular in our previous study (17), six increased after *SRSF6* KD in normoxia (Supplementary Figure S5C).

To assess whether SRSF6 OE attenuates exon skipping and circularization in hypoxia, we selected from our WT dataset six exon skipping events and three hypoxia-induced circRNAs. Except for *CSPP1* exon 5, all selected skipped or circularized exons contained numerous SRSF6-binding motifs (GAA; Supplementary Figure S5D, E). RT-PCR confirmed the skipping of those exons under normoxia, their increased skipping under hypoxia and, in all cases, the attenuation of their hypoxia-driven skipping in SRSF6 OE cells. Strikingly, skipping of those exons was also attenuated in ΔPCE cells, except for *CSPP1* exon 5 (Figure 5F; Supplementary Figure S5F). Similarly, the formation of *circRTN4* and *circPLOD2*, but not of *circMAN1A2*, was attenuated in SRSF6 OE cells (Supplementary Figure S5G).

Together, these observations suggest that deregulated, high levels of SRSF6 in hypoxia promote the inclusion of specific target exons into mature transcripts and prevent exon skipping and circularization. The reduction of SRSF6 in hypoxia thus appears crucial to allow for AS and back-splicing to generate splice isoforms that could play roles in the adaptation to hypoxia.

SRSF6 binding to 3′ splice sites is reduced in hypoxia

To further investigate the regulatory mechanism of SRSF6-mediated AS in hypoxia, we performed iCLIP (69). Low SRSF6–GFP-expressing cells were grown under normoxic and hypoxic conditions (4 h and 24 h, 0.2% O_2) and iCLIP libraries were prepared in three replicates (Figure 6A;, Supplementary Figure S6A). The earlier time point of 4 h was chosen to compare the binding of SRSF6 to hypoxia-induced transcripts, since HIF1α levels are maximal at this point, while SRSF6 levels are not yet reduced (Figure 6A). iCLIP reads were processed according to (47) to obtain unique SRSF6 cross-link events. Peak calling (49) on the cross-link events from pooled replicates and stringent filtering identified 18 956 reproducible SRSF6-binding sites (7 nt width) in 3145 target genes.

A total of 85.6% (16 234) of the binding sites mapped to protein-coding genes, where binding was most enriched in CDSs (Supplementary Figure S6B, C). A purine-rich consensus binding motif (GAAGAA) emerged from the CDS regions (Figure 6C; Supplementary Figure S6D), which was highly similar to that obtained in mouse P19 cells and human pancreatic β-cells (56,57). However, within intronic sequences, the SRSF6-binding motif was enriched in uridines, suggesting that SRSF6 also binds to polypyrimidine tracts (Figure 6C; Supplementary Figure S6D). SR proteins normally promote splicing through binding to exonic splicing enhancer (ESE) sequences, but they can also inhibit the inclusion of alternative exons through binding to intronic splicing silencer (ISS) sequences (70,71). Indeed, a pronounced peak of SRSF6 binding was visible in introns, 12–13 nt upstream of 3′ splice sites of CEs that are skipped in hypoxia in SRSF6 OE cells (Figure 6D, red arrows). This intronic peak was not visible in more included exons and was strongly reduced at 24 h hypoxia, while SRSF6 binding to the exons flanking those CEs did not change. A similar peak disappearing in hypoxia was visible at 3′ splice sites of downstream exons (Figure 6D, red arrows). SRSF6 bound generally more in skipped compared with more included exons, and binding decreased after 24 h of hypoxia (Figure 6D, blue arrows). Similar hypoxia-sensitive peaks were observed at exons, which are exclusively regulated in SRSF6 OE cells (not in the WT; Supplementary Figure S6E). When we mapped cross-link events on CEs whose skipping/inclusion was attenuated in SRSF6 OE cells (Figure 5D), no clear difference in binding between skipped and more included exons or between normoxia and hypoxia was observed (Supplementary Figure S6F). Regulated minigenes more often contain SRSF6-binding sites than non-regulated minigenes, and also show higher binding site numbers. However, only 23% of all regulated minigenes contain SRSF6-binding sites. Similarly, of the eight validated attenuated skipped exons and circRNAs, only two—*BORA* exon 3 and *MDM4* exon 6—showed a clear difference in SRSF6 binding between normoxia and hypoxia (Supplementary Figure S7B, C).

Altogether our data suggest that SRSF6 promotes inclusion of alternative exons in normoxia by binding directly to the alternative exons or upstream of 3′ splice sites. Both SRSF6 binding modes are reduced in hypoxia, which may contribute to the observed skipping of the alternative exons in hypoxia. However, only a small fraction of all skipped exons showed reduced SRSF6 binding in hypoxia, thus additional mechanisms and factors must contribute to global exon skipping in hypoxia.

SRSF6 down-regulation in hypoxia causes nuclear speckle dispersal

Beside its role in AS regulation, SRSF6 is also a core protein of NSs (72). Interestingly, NSs disperse during hypoxia (Figure 7A, B; Supplementary Figure S8A). Using the markers SC35 and SRRM2 in immunofluorescence ex-

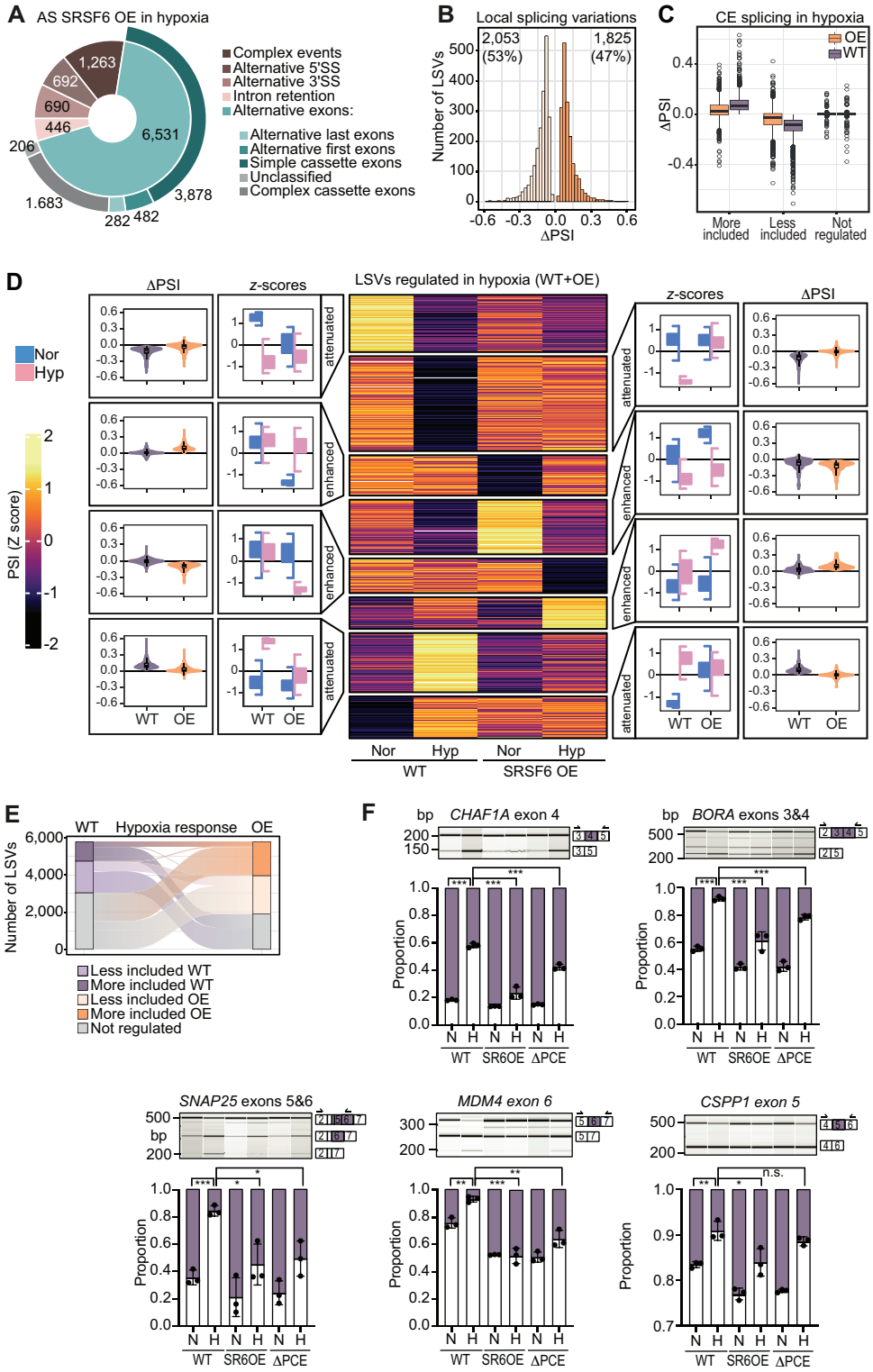

Figure 5. Maintaining high SRSF6 levels in hypoxia impairs exon skipping. (**A**) Pie chart displaying the total number of significantly regulated LSVs in hypoxic (0.2% O_2) compared with normoxic (21% O_2) SRSF6 OE HeLa cells separated into distinct splice events; $n = 2$ replicates per condition. (**B**) Histogram showing the difference in inclusion junction usage (ΔPSI) of regulated simple CEs in hypoxic SRSF6 OE cells. Numbers of more or less included exons are given above. (**C**) Box plot displaying the ΔPSI values of LSVs, separated by more included, less included and not regulated in hypoxic WT cells, in WT cells after 24 h hypoxia and the corresponding values in SRSF6 OE cells. (**D**) Heatmap and box plots comparing the LSVs in hypoxia between WT and SRSF6 OE cells. Clusters were defined by *k*-means clustering ($k = 8$). Outer violin plots and inner box plots show the distribution of ΔPSI values (Hyp-Nor) and mean *z*-scores, respectively, within each cluster. (**E**) Sankey plot tracing the regulated LSVs between WT and SRSF6 OE cells. (**F**) Semi-quantitative RT-PCR splicing gel analysis of *CHAF1A*, *BORA*, *SNAP25*, *MDM4* and *CSPP1* in WT, SRSF6 OE and SRSF6ΔPCE cells in normoxia and hypoxia. Alternative CEs are marked in purple. Black arrows above the exons indicate the primer positions. Size markers (in bp) are shown on the left side of each gel picture. Relative proportions of exon-including isoforms, shown in purple, quantified from three independent experiments.

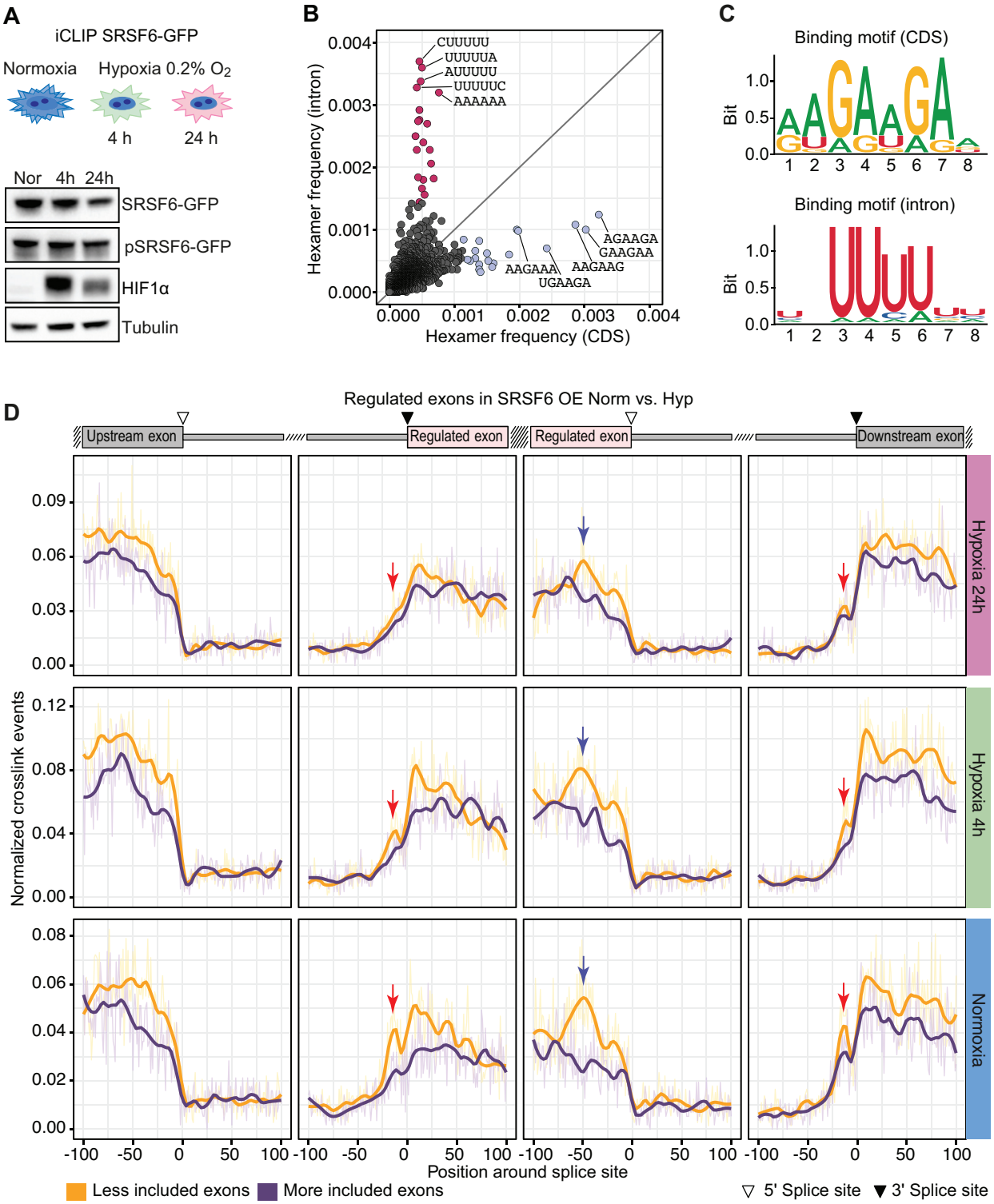

Figure 6. SRSF6 binding to 3′ splice sites is reduced in hypoxia. (**A**) Representative western blot from SRSF6–GFP cells grown in normoxia and 4 h and 24 h hypoxia. mAb104 antibody was used to detect phosphorylated SRSF6–GFP (pSRSF6–GFP), and anti-SRSF6 antibody to detect total SRSF6 protein. Anti-HIF1α antibody was used to control for successful hypoxia treatment, and tubulin was used as loading control. (**B**) Hexamer frequencies in a 101 nt window around SRSF6-binding sites in CDSs and introns. (**C**) SRSF6-binding motif in CDS and introns derived from the 10 most enriched hexamers. (**D**) RNA map of normalized SRSF6 cross-link events from different conditions (normoxia, 4 h hypoxia and 24 h hypoxia) around the 3′ and 5′ splice sites of exons that are regulated by hypoxia in SRSF6 OE cells, as well as flanking upstream and downstream exons. Red arrows highlight positions where SRSF6 binding diverges at the 3′ splice sites and blue arrows where binding diverges within the alternative exons.

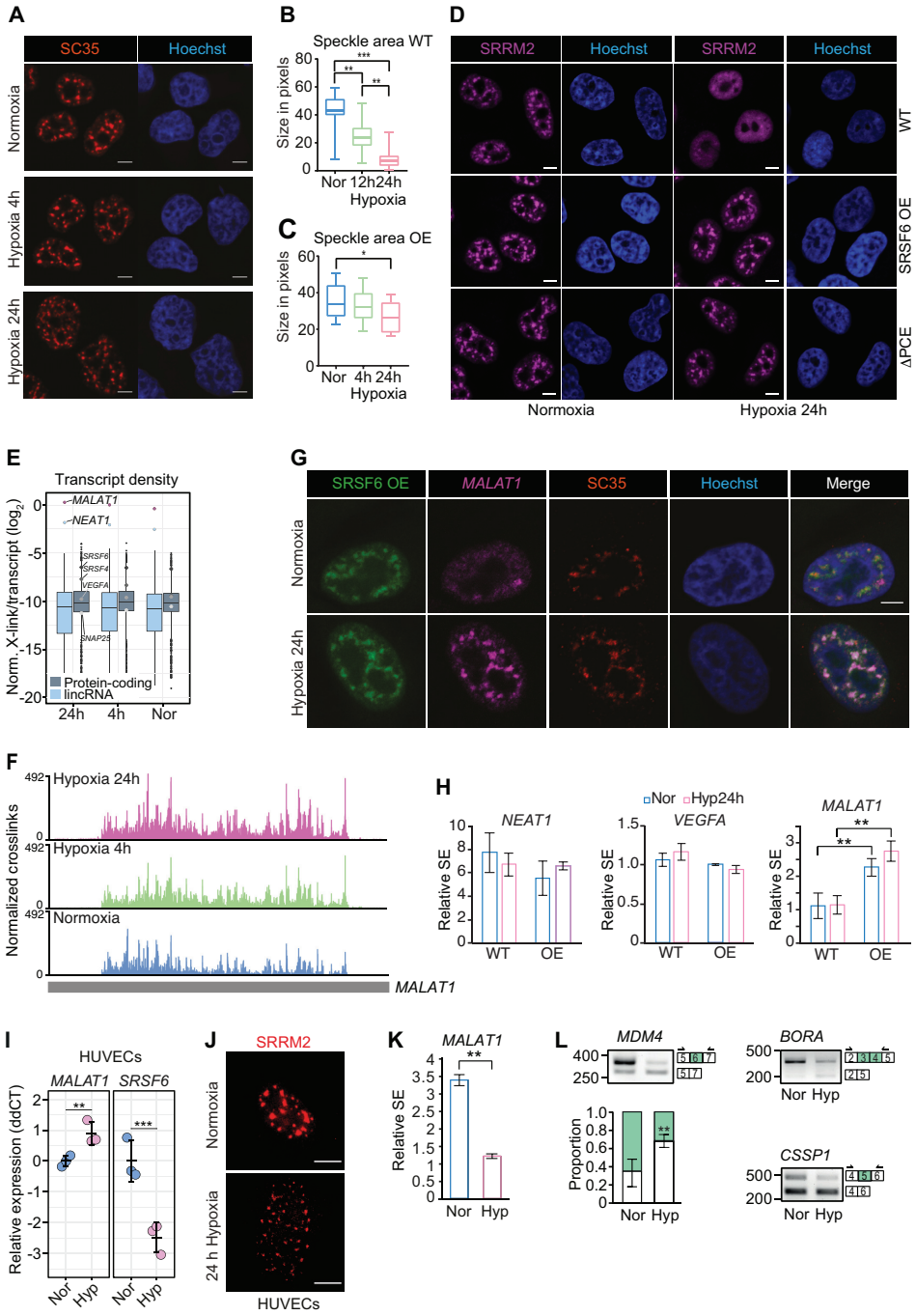

Figure 7. SRSF6 down-regulation in hypoxia allows NS dispersal and increases the nuclear mobility of *MALAT1*. (**A**) Representative immunofluorescence (IF) microscopy images showing the dispersal of NSs in WT cells in hypoxia (4 h and 24 h). NSs were labeled with α-SC35 (red) and nuclei with Hoechst (blue). (**B** and **C**) Box plots showing the area of NSs quantified from 100 WT cells (B) and 100 SRSF6 OE cells (C) grown in normoxia (Nor), and 4, 12 and 24 h hypoxia. (**D**) Representative IF microscopy images comparing the distribution of NSs in WT, SRSF6 OE and SRSF6ΔPCE cells between normoxic and hypoxic conditions (24 h). NSs were labeled with α-SRRM2 (magenta). (**E**) Boxplot showing the density of normalized SRSF6 cross-link events (number of X-links per transcript) on *MALAT1* and *NEAT1* on a $\log_2$ scale. (**F**) Browser shot showing the distribution of normalized SRSF6 cross-link events on the *MALAT1* transcript in normoxia and hypoxia (4 h and 24 h). (**G**) Representative RNA FISH and IF microscopy images comparing the distribution and levels of *MALAT1* in SRSF6 OE cells between normoxic and hypoxic conditions (24 h). SRSF6–GFP (green), *MALAT1* (magenta), NSs labeled with α-SC35 (red), Hoechst (blue) and the merge of all channels are shown. (**H**) RT–qPCR to quantify and compare the relative semi-extractability (SE) of *MALAT1* in WT and SRSF6 OE cells in normoxia and hypoxia ($n = 3$). Shown for comparison are *NEAT1*, which is highly semi-extractable in hypoxia and normoxia (~7-fold) (75), and *VEGFA* that is not semi-extractable which served as controls. (**I**) RT–qPCR to quantify the levels of *SRSF6* and *MALAT1* in HUVECs in normoxia and hypoxia ($n = 3$). (**J**) Representative IF microscopy image showing NS dispersal in HUVECs in hypoxia (24 h), labeled with α-SRRM2 (red). (**K**) RT–qPCR to quantify and compare the relative SE of *MALAT1* in HUVECs in normoxia and hypoxia ($n = 3$). (**L**) Semi-quantitative RT-PCR splicing gel showing inclusion of *MDM4* exon 6, *BORA* exons 2 and 3 and *CSPP1* exon 5 in HUVECs under normoxia and hypoxia. Alternative CAs are labeled in green; $n = 3$ independent experiments. All data: Student's *t*-test: **P*-value <0.05, ***P*-value <0.01, ****P*-value <0.001. Scale bars = 5 μm.

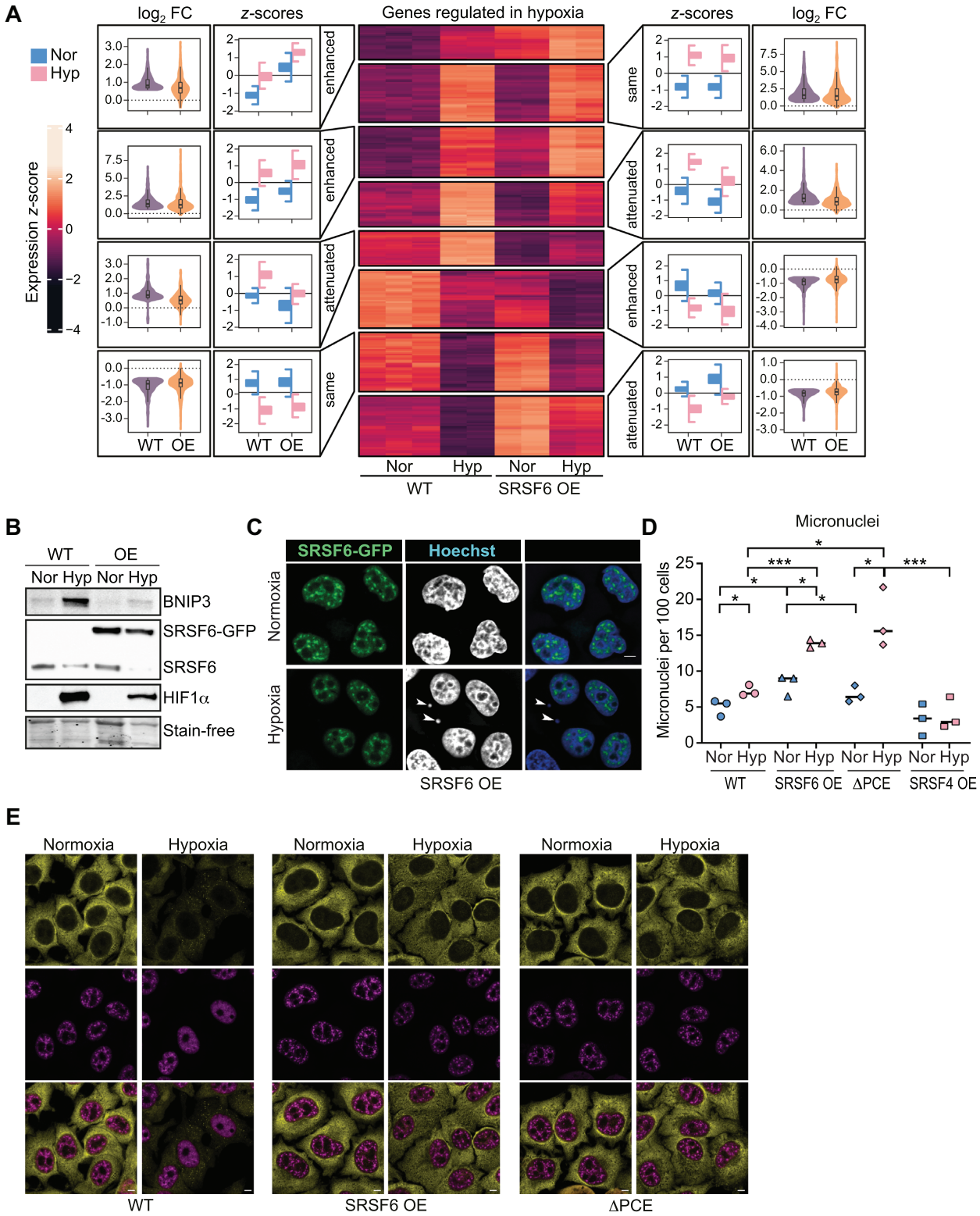

Figure 8. Maintaining high levels of SRSF6 in hypoxia suppresses the stress response and causes genomic instability. (**A**) Heatmap and box plots comparing the differential gene regulation in hypoxia between WT and SRSF6 OE cells. Clusters defined by *k*-means clustering ($k = 8$). Outer violin plots and inner box plots show the distribution of $\log_2$-fold changes (Hyp/Nor) and mean *z*-scores, respectively, within each cluster. (**B**) Western blot comparing the levels of HIF1α, the HIF1α-regulated protein BNIP3, SRSF6 and SRSF6–GFP in WT and SRSF6 OE cells in normoxia and hypoxia (24 h). (**C**) Fluorescence microscopy images of SRSF6 OE cells in normoxia and hypoxia (24 h) showing increased formation of micronuclei (white arrows). GFP, green; Hoechst, blue, and gray in the single-channel picture. (**D**) Number of micronuclei per 100 cells comparing WT, SRSF6 OE, SRSF4 OE and SRSF6ΔPCE cells in normoxia and hypoxia; $n = 4$ (>100 cells/experiment). (**E**) Representative IF microscopy images comparing NS dispersal and stress granule occurrence in WT, SRSF6 OE and SRSF6ΔPCE cells between normoxic and hypoxic conditions (24 h). NSs were labeled with α-SRRM2 (magenta), and stress granules with α-G3BP1 (yellow). All data: Student's *t*-test, **P*-value <0.05, ***P*-value <0.01, ****P*-value <0.001. Scale bars = 5 μm.

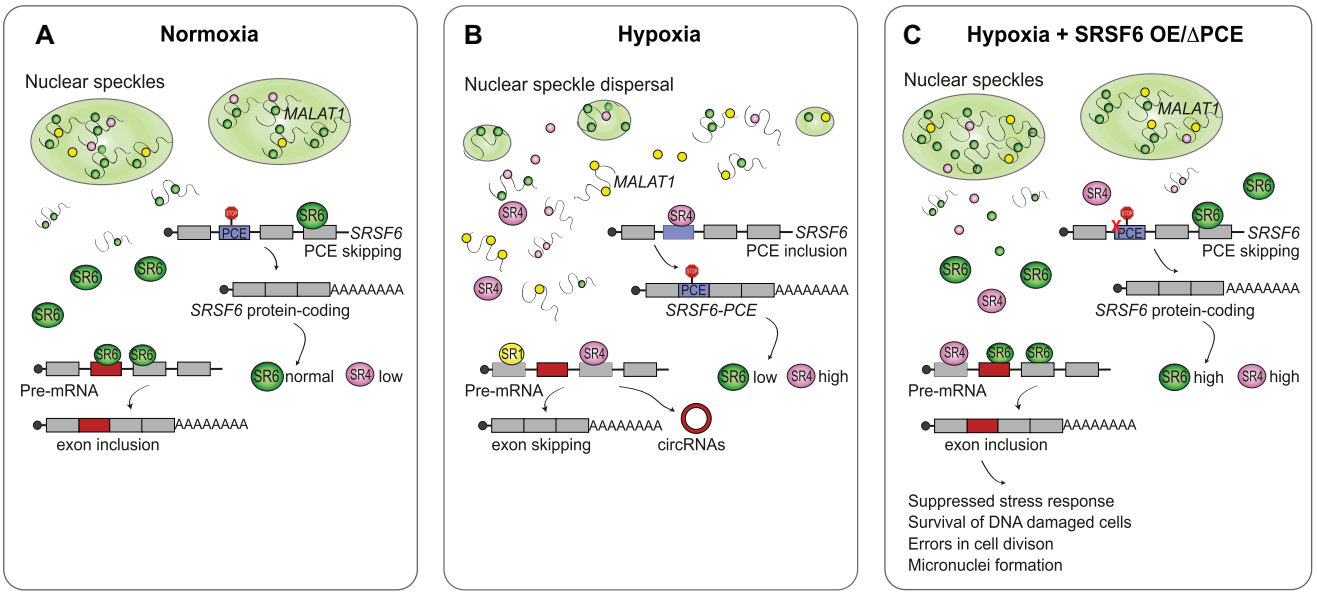

Figure 9. Model of hypoxia regulation by SRSF6 and SRSF4. (**A**) Normoxia**:** normal levels of SRSF6 and low levels of SRSF4 promote splicing of the protein-coding isoform of *SRSF6* and inclusion of alternative exons, either by binding directly to alternative exons and to 3′ splice sites or by preserving nuclear speckles. (**B**) Hypoxia**:** SRSF4 is up-regulated and SRSF6 is down-regulated in hypoxia. High SRSF4 levels promotes inclusion of the *SRSF6* PCE, which decreases the levels of coding *SRSF6* transcripts and SRSF6 protein. Low SRSF6 levels promote exon skipping, either through reduced binding to target exons or through the dispersal of nuclear speckles. This results in the release of splicing factors, such as SRSF1, and *MALAT1,* which can now bind to strong splice sites and promote exon skipping. (**C**) Hypoxia and SRSF6 OE/ΔPCE**:** high SRSF6 levels in hypoxia, either through SRSF6 OE or by preventing PCE inclusion counteract exon skipping by binding to target exons and by impairing nuclear speckle dispersal, which sequesters splicing factors and *MALAT1*. This leads to the suppression of the stress response and the proliferation of cells with DNA damage, which leads to errors in cell division and micronuclei formation.

periments, NSs looked smaller and more numerous or completely disappeared in hypoxia in WT and SRSF4 OE cells, where SRSF6 levels are low. However, NS dispersal was not observed after $CoCl_2$ treatment (Supplementary Figure S8B, C), where SRSF6 levels remain unchanged (Supplementary Figure S3A–D), and it was also strongly reduced in SRSF6 OE or SRSF6ΔPCE cells, where SRSF6 levels remain high in hypoxia (Figure 7C, D). These data strongly suggest that SRSF6 reduction in hypoxia is required for NS dispersal. SRSF6 reduction and NS dispersal under hypoxia should increase the availability of splicing factors in the nucleoplasm. Uncontrolled binding and activation of strong splice sites should in turn disfavor the recognition of alternative exons with weak splice sites (72,73) and thus contribute to the observed exon skipping in hypoxia.

NS dispersal should also affect the mobility of the long non-coding RNA (lncRNA) *MALAT1*, which resides in these condensates (74). According to our iCLIP data, *MALAT1* was the transcript with the highest binding density of SRSF6, which further increased in hypoxia (Figure 7E, F). SRSF6 densely coated *MALAT1* along its entire length, supporting a direct role for SRSF6 in tethering this lncRNA to NSs (Figure 7F). The levels of *MALAT1* increased in hypoxia and the lncRNA was detectable in NSs and in the nucleoplasm when SRSF6 levels were low (Supplementary Figure S8D, F, G). In contrast, in SRSF6 OE cells, *MALAT1* was exclusively detectable in NSs, where it completely co-localized with SRSF6 and the NS marker SC35 (Figure 7G; Supplementary Figure S8G, H). This suggests that down-regulation of SRSF6 and NS dispersal in hypoxia increase the nuclear mobility of *MALAT1*.

To test this further, we quantified the extractability of *MALAT1,* which correlates with the extent of sequestration in NSs or in other phase-separated biomolecular condensates (75,76). To do this, we pre-heated cell lysates in Trizol (10 min at 55°C) to strip-off all bound proteins (75) prior to RNA extraction. *MALAT1* was indeed much less extractable without heat treatment in hypoxic SRSF6 OE cells (2.8-fold increase in heat-treated versus control samples) compared with WT cells, where *MALAT1* was almost fully extractable without heat treatment (1.2-fold increase, Figure 7H). In line with SRSF6 regulating *MALAT1* extractability, *SRSF6* knockdown led to an apparent increase in *MALAT1* levels in normoxia similar to its increase in hypoxia (Supplementary Figure S8D, E). In contrast, SRSF6 OE attenuated the apparent *MALAT1* levels in hypoxia (Supplementary Figure S8D, G). Our data suggest that high levels of SRSF6 in hypoxia prevent NS dispersal and global exon skipping, and decrease the extractability and nuclear mobility of *MALAT1*.

To test whether hypoxia-mediated SRSF6 reduction and NS dispersal also occur in non-cancerous cells, we subjected HUVECs to 24 h of hypoxia (0.2% O_2). *SRSF6* mRNA levels were ∼5-fold decreased in hypoxia (Figure 7I), similar to HeLa cells, and SRSF6 protein levels were reduced by ∼50% (Supplementary Figure S8I). NSs were also dispersed in hypoxia (Figure 7J), and *MALAT1* was fully extractable in this condition (Figure 7K). In contrast, in normoxia, *MALAT1* was 3.4-fold less extractable (Figure 7K). Out of six tested splicing targets, three showed the same splicing pattern as in HeLa cells in hypoxia (Figure 7L) and *MALAT1* levels also increased (Figure 7I). This suggests

that the acute hypoxia response mediated by SRSF6 reduction is conserved in HeLa cells and HUVECs, but the outcome of AS might be cell type specific and probably depends on the transcriptome and the interplay of SRSF6 with other splicing-regulatory proteins (10,17).

Altogether, our data suggest that the reduction of SRSF6 in hypoxia allows NS dispersal, which results in the release of stored splicing factors including *MALAT1*. This promotes exon skipping and AS of stress-relevant genes and provides an additional layer of SRSF6-mediated gene regulation during hypoxic stress beyond its direct impact on AS.

Maintaining high levels of SRSF6 in hypoxia suppresses the stress response, and causes DNA damage and genomic instability

To assess the impact of high SRSF6 levels in hypoxia on cell survival and adaptation, we performed differential gene expression analyses. Interestingly, SRSF6 OE cells showed fewer differentially expressed genes (DEGs) in hypoxia compared with WT cells (582 down, 1409 up), suggesting that the hypoxia response is partially suppressed in SRSF6 OE cells. Clustering of gene expression patterns across conditions identified several clusters of DEGs in which the hypoxia-induced up- or down-regulation observed in WT cells was attenuated in SRSF6 OE cells (Figure 8A). Attenuated biological processes included 'response to oxygen' and 'cellular response to DNA damage' and 'regulation of the stress response' (Supplementary Figure S9A). Indeed, the levels of HIF1α and the HIF1α-induced protein BNIP3 (77) were lower in SRSF6 OE cells compared with WT cells under hypoxia (Figure 8B). Consistent with a suppressed DNA damage response, SRSF6 OE cells showed large foci stained for phosphorylated Ser139 of histone H2AX (pH2AX), a marker for DNA double-strand breaks (Supplementary Figure S9B). SRSF6 OE cells also displayed significantly higher numbers of micronuclei compared with the WT under hypoxia (Figure 8C, D), which are indicators of chromosomal instability in cells with damaged DNA (78). Importantly, PCE inactivation in the *SRSF6* gene elicited the same chromosomal instability phenotype (Figure 8C, D). Conversely, SRSF4 OE completely prevented formation of micronuclei, in line with the strongest down-regulation of SRSF6 levels in hypoxic conditions in these cells. Interestingly, stress granules, which were clearly visible in hypoxia in WT cells, were completely suppressed in SRSF6 OE and ΔPCE cells, in line with an inhibition of the general stress response by high SRSF6 levels (Figure 8E).

Other processes that no longer responded to hypoxia in SRSF6 OE cells were 'cell cycle', 'cell migration' and 'negative regulation of cell proliferation' (Supplementary Figure S9A). Proliferation assays using EdU confirmed that SRSF6 OE cells replicated slightly faster than WT cells under hypoxia (Supplementary Figure S9C, D).

Thus, SRSF6 OE fundamentally disturbs the hypoxia response of a large number of hypoxia-regulated genes [3120 out of 4410 (71%) DEGs in hypoxic WT cells] by either attenuation or enhancement. Altogether, our data suggest that deregulated, high levels of SRSF6 in hypoxia due to impaired PCE inclusion suppress general stress response pathways and lead to higher proliferation and genomic instability under extended periods of hypoxia.

DISCUSSION

Hypoxia induces massive changes in gene expression, including AS and circRNA formation, to allow cells to adapt to the lack of oxygen (8–13,16,17,79). In normal cells, the hypoxia response serves to sustain viability, to repair associated damage and to restore cellular homeostasis. In tumor cells, hypoxia-induced AS also plays clear roles in metastatic progression and was shown to activate oncogenes, inactivate tumor suppressors, enhance proliferation and angiogenesis, evade programmed cell death, modulate the immune and inflammatory response, and cause adaptive metabolic reprogramming, EMT, invasion and genetic instability [reviewed in (14)].

Few proteins have been characterized as hypoxia-related splicing regulators, and the underlying mechanisms are often not understood (18). Here, we identify the SR protein SRSF6 as a key factor that controls the adaptive AS response in hypoxia (Figure 9). Using HeLa cells, we show here that SRSF6 activities are reduced in acute hypoxia through a reduction of total protein levels and enhanced SRSF6 phosphorylation. The former is achieved through the inclusion of a PCE in its own transcript at the expense of the protein-coding *SRSF6* isoform. PCE inclusion is mainly promoted by SRSF4, whose levels and activity increase in hypoxia, and SRSF6 itself, which both bind massively to the PCE. Our data suggest that SRSF6 inactivation in hypoxia serves a dual purpose: (i) it allows for skipping of direct SRSF6 target exons and splicing of specific circRNAs, which may fulfill specific functions in hypoxia adaptation; and (ii) it causes the dispersal of NSs during hypoxia, which releases stored splicing factors and is expected to cause global changes in gene expression and splicing as is observed in hypoxia.

NSs are scaffolded by SRRM2 and SON, but NS cohesion is provided through many RBPs containing arginine-rich mixed-charge domains, such as RS domains (80,81). Phosphorylation of serine residues in RS domains increases their negative charge and reduces NS cohesion. Accordingly, NS dispersal can be induced by overexpressing the SR protein kinase CLK1 (80,82), and this was shown to enhance the splicing of specific introns (82). We propose that NS dispersal in hypoxia is essential to reprogram gene expression and adapt to this stress condition. SRSF6 probably plays a central role in NS cohesion because (i) it has a long RS domain and is found in the core of nuclear speckles, (ii) its levels are reduced in hypoxia and residual SRSF6 is proportionally more phoshorylated and (iii) maintaining high SRSF6 levels in hypoxia, either by overexpression or by removing the 3′ splice site of its PCE, severely impairs NS dispersal and profoundly disturbs the hypoxia adaption program; it prevents exon skipping and circRNA formation, attenuates the expression of many genes and sequesters *MALAT1* in these condensates. As a consequence, stress responses and check points are impaired and DNA damage accumulates, promoting chromosomal instability, which is a hallmark of metastatic progression of tumor cells (14,83–85). In line with this, colorectal, skin, lung

and breast cancer show aberrantly high levels of SRSF6, and this was demonstrated to promote proliferation, evasion of cell death, tumor progression, EMT and metastasis (31–34,86).

Thousands of transcripts are alternatively spliced in hypoxia, but their identity depends on the cell type (10,17). In hypoxic HeLa cells, the most commonly occurring type of AS event was the splicing of alternative CEs, similar to observations with Hep3B cells (13). We have identified and validated several novel hypoxia-induced splicing events. For instance, hypoxia leads to skipping of exons 3 and 4 in *BORA*, which would generate a BORA protein isoform that lacks 50 amino acids near the N-terminus (Δaa112–162). BORA is a cell cycle regulator with important functions in cell cycle progression after mitotic arrest due to the DNA damage response (87). Mutations in *BORA* that impair its phosphorylation were shown to inhibit its activity and cause cell cycle arrest (88). Similarly, skipping of exon 6 in *MDM4* generates the shorter isoform *MDM4-S* in hypoxia, resulting in a protein variant with increased activity towards repressing the tumor suppressor p53 (89). *MDM4-S* is often up-regulated in cancer cells as a mechanism to inactivate apoptosis signaling pathways. MDM4 was also shown to promote DNA replication, inhibit the kinase mTOR and maintain genome stability in p53-deficient cancer cells (90–92). In another example, exon skipping in *CHAF1A* leads to the formation of a protein isoform that lacks the histone interaction domain and thus should impair the DNA damage response and chromatin assembly in hypoxia (93). Hypoxia also changes the splicing of *SNAP25*. The encoded SNAP25 protein plays a role in synaptic vesicle trafficking (94) and is needed for the uptake of anti-angiogenic and pro-apoptotic proteins through endosomes in endothelial cells (95), which might be used by cancer cells as well. AS in hypoxia increases the *SNAP25b* isoform, which is protein coding but has a negative effect on the function of *SNAP25a* (94). In all described cases, exon skipping requires low SRSF6 levels, highlighting the importance of SRSF6 reduction as an additional layer of hypoxia adaptation.

Interestingly, hypoxia also promotes inclusion of exon 4 in the SR protein kinase *CLK1* transcript, which leads to elevated levels of full-length CLK1 (29). Enhanced CLK1 levels were shown to cause dispersal of NSs (69). Our data suggest that SRSF6 binds strongly to exon 4 in hypoxia but SRSF6 OE attenuates exon 4 inclusion in hypoxia. This attenuation may contribute to the observed impairment of NS dispersal.

SRSF6 PCE inclusion in hypoxia was recently reported in pancreatic cancer organoids and proposed to be HIF1 dependent (96). Our data suggest that *SRSF6* PCE splicing is independent of HIF1 stabilization and rather depends on the general hypoxia stress response, including phosphorylation of SRSF6. A recent genome-wide CRISPR screen identified the SRSF6 PCE among a subset of ultraconserved PCEs with clinically relevant tumor suppressor activities (97). We propose that the ultraconserved PCE of SRSF6 acts as tumor suppressor and that its inclusion in hypoxia is crucial to reduce SRSF6 levels, which may prevent tumor cells from entering the metastatic route of hypoxia adaptation.

DATA AVAILABILITY

All sequencing data are available in the Gene Expression Omnibus (GEO) under the SuperSeries accession number GSE198313. The collection includes the RNA-seq data from SRSF6 OE HeLa cells (GSE198308) as well as the iCLIP data for SRSF6–GFP in HeLa cells under normoxia and under 4 h and 24 h hypoxia (GSE198309).

The mass spectrometry proteomics data are available upon request.

SUPPLEMENTARY DATA

Supplementary Data are available at NAR Online.

ACKNOWLEDGEMENTS

We thank A. Dahl for advice and sequencing of the iCLIP libraries, I. de los Mozos, J. Ule and T. Curk for support and advice on iCLIP data analyses, A. Eberle and A.K. Neuhoff for their help in generating and characterizing the CRISPR mutants, D. Homann for the HUVEC images, and M. Klostermann for bioinformatics support.

Author contributions: M.M.M., K.Z. and C.deO.F.M. designed the experiments. C.deO.F.M., F.M., M.C.H.C., B.A., I.W., N.B. and M.S. performed the experiments. M.B., A.D.L., I.W., M.K., K.Z., A. Brezski and M.M.M. performed the bioinformatics analyses. A. Bremm, N.J. and S.D. contributed advice, reagents and hypoxia chambers. Figures were prepared by C.deO.F.M., M.C.H.C., M.B., M.K., B.A., K.Z. and M.M.M.. The manuscript was written by C.deO.F.M., F.M., K.Z. and M.M.M.

FUNDING

We are grateful for funding from the Deutsche Forschungsgemeinschaft [TRR267-Z02 to I.W., CEF-MC, ECCPS, CPI, TRR267-A03 and SFB902-B13 to M.M.M., ECCPS, CPI, TRR267-A01 and SFB902-B13 to K.Z., and TRR267-A01, ECCPS and CPI to S.D.].

Conflict of interest statement. None declared.

REFERENCES

1. Lee,P., Chandel,N.S. and Simon,M.C. (2020) Cellular adaptation to hypoxia through hypoxia inducible factors and beyond. *Nat. Rev. Mol. Cell Biol.*, **21**, 268–283.
2. Nakazawa,M.S., Keith,B. and Simon,M.C. (2016) Oxygen availability and metabolic adaptations. *Nat. Rev. Cancer*, **16**, 663–673.
3. de Heer,E.C., Jalving,M. and Harris,A.L. (2020) HIFs, angiogenesis, and metabolism: elusive enemies in breast cancer. *J. Clin. Invest.*, **130**, 5074–5087.
4. Kaelin,W.G. Jr and Ratcliffe,P.J. (2008) Oxygen sensing by metazoans: the central role of the HIF hydroxylase pathway. *Mol. Cell*, **30**, 393–402.
5. Krock,B.L., Skuli,N. and Simon,M.C. (2011) Hypoxia-induced angiogenesis: good and evil. *Genes Cancer*, **2**, 1117–1133.
6. Schito,L. and Semenza,G.L. (2016) Hypoxia-inducible factors: master regulators of cancer progression. *Trends Cancer*, **2**, 758–770.
7. Semenza,G.L. (2012) Hypoxia-inducible factors in physiology and medicine. *Cell*, **148**, 399–408.
8. Bowler,E., Porazinski,S., Uzor,S., Thibault,P., Durand,M., Lapointe,E., Rouschop,K.M.A., Hancock,J., Wilson,I. and Ladomery,M. (2018) Hypoxia leads to significant changes in alternative splicing and elevated expression of CLK splice factor kinases in PC3 prostate cancer cells. *BMC Cancer*, **18**, 355.

9. Brady,L.K., Wang,H., Radens,C.M., Bi,Y., Radovich,M., Maity,A., Ivan,C., Ivan,M., Barash,Y. and Koumenis,C. (2017) Transcriptome analysis of hypoxic cancer cells uncovers intron retention in EIF2B5 as a mechanism to inhibit translation. *PLoS Biol.*, **15**, e2002623.
10. Fischer,S., Di Liddo,A., Taylor,K., Gerhardus,J.S., Sobczak,K., Zarnack,K. and Weigand,J.E. (2020) Muscleblind-like 2 controls the hypoxia response of cancer cells. *RNA*, **26**, 648–663.
11. Han,J., Li,J., Ho,J.C., Chia,G.S., Kato,H., Jha,S., Yang,H., Poellinger,L. and Lee,K.L. (2017) Hypoxia is a key driver of alternative splicing in human breast cancer cells. *Sci. Rep.*, **7**, 4108.
12. Peciuliene,I., Vilys,L., Jakubauskiene,E., Zaliauskiene,L. and Kanopka,A. (2019) Hypoxia alters splicing of the cancer associated Fas gene. *Exp. Cell. Res.*, **380**, 29–35.
13. Sena,J.A., Wang,L., Heasley,L.E. and Hu,C.J. (2014) Hypoxia regulates alternative splicing of HIF and non-HIF target genes. *Mol. Cancer Res.*, **12**, 1233–1243.
14. Farina,A.R., Cappabianca,L., Sebastiano,M., Zelli,V., Guadagni,S. and Mackay,A.R. (2020) Hypoxia-induced alternative splicing: the 11th hallmark of cancer. *J. Exp. Clin. Cancer Res.*, **39**, 110.
15. Peiris-Pages,M. (2012) The role of VEGF 165b in pathophysiology. *Cell Adh. Migr.*, **6**, 561–568.
16. Boeckel,J.N., Jae,N., Heumüller,A.W., Chen,W., Boon,R.A., Stellos,K., Zeiher,A.M., John,D., Uchida,S. and Dimmeler,S. (2015) Identification and characterization of hypoxia-regulated endothelial circular RNA. *Circ. Res.*, **117**, 884–890.
17. Di Liddo,A., de Oliveira Freitas Machado,C., Fischer,S., Ebersberger,S., Heumüller,A.W., Weigand,J.E., Müller-McNicoll,M. and Zarnack,K. (2019) A combined computational pipeline to detect circular RNAs in human cancer cells under hypoxic stress. *J. Mol. Cell Biol.*, **11**, 829–844.
18. Kanopka,A. (2017) Cell survival: interplay between hypoxia and pre-mRNA splicing. *Exp. Cell. Res.*, **356**, 187–191.
19. Manley,J.L. and Krainer,A.R. (2010) A rational nomenclature for serine/arginine-rich protein splicing factors (SR proteins). *Genes Dev.*, **24**, 1073–1074.
20. Änkö,M.L. (2014) Regulation of gene expression programmes by serine–arginine rich splicing factors. *Semin. Cell Dev. Biol.*, **32**, 11–21.
21. Wegener,M. and Müller-McNicoll,M. (2019) View from an mRNP: the roles of SR proteins in assembly, maturation and turnover. *Adv. Exp. Med. Biol.*, **1203**, 83–112.
22. Zheng,X., Peng,Q., Wang,L., Zhang,X., Huang,L., Wang,J. and Qin,Z. (2020) Serine/arginine-rich splicing factors: the bridge linking alternative splicing and cancer. *Int. J. Biol. Sci.*, **16**, 2442–2453.
23. Wagner,R.E. and Frye,M. (2021) Noncanonical functions of the serine–arginine-rich splicing factor (SR) family of proteins in development and disease. *Bioessays*, **43**, e2000242.
24. An,Y., Zou,Y., Cao,Y., Yao,M., Ma,N., Wu,Y., Yang,J., Liu,H. and Zhang,B. (2019) The nuclear GSK-3beta regulated post-transcriptional processing of mRNA through phosphorylation of SC35. *Mol. Cell. Biochem.*, **451**, 55–67.
25. Boutz,P.L., Bhutkar,A. and Sharp,P.A. (2015) Detained introns are a novel, widespread class of post-transcriptionally spliced introns. *Genes Dev.*, **29**, 63–80.
26. Feng,Y., Chen,M. and Manley,J.L. (2008) Phosphorylation switches the general splicing repressor SRp38 to a sequence-specific activator. *Nat. Struct. Mol. Biol.*, **15**, 1040–1048.
27. Goldammer,G., Neumann,A., Strauch,M., Müller-McNicoll,M., Heyd,F. and Preussner,M. (2018) Characterization of cis-acting elements that control oscillating alternative splicing. *RNA Biol*, **15**, 1081–1092.
28. Leva,V., Giuliano,S., Bardoni,A., Camerini,S., Crescenzi,M., Lisa,A., Biamonti,G. and Montecucco,A. (2012) Phosphorylation of SRSF1 is modulated by replicational stress. *Nucleic Acids Res.*, **40**, 1106–1117.
29. Jakubauskiene,E., Vilys,L., Makino,Y., Poellinger,L. and Kanopka,A. (2015) Increased serine–arginine (SR) protein phosphorylation changes pre-mRNA splicing in hypoxia. *J. Biol. Chem.*, **290**, 18079–18089.
30. Zhou,L., Guo,J. and Jia,R. (2019) Oncogene SRSF3 suppresses autophagy via inhibiting BECN1 expression. *Biochem. Biophys. Res. Commun.*, **509**, 966–972.
31. Cohen-Eliav,M., Golan-Gerstl,R., Siegfried,Z., Andersen,C.L., Thorsen,K., Orntoft,T.F., Mu,D. and Karni,R. (2013) The splicing factor SRSF6 is amplified and is an oncoprotein in lung and colon cancers. *J. Pathol.*, **229**, 630–639.
32. Kong,J., Sun,W., Li,C., Wan,L., Wang,S., Wu,Y., Xu,E., Zhang,H. and Lai,M. (2016) Long non-coding RNA LINC01133 inhibits epithelial–mesenchymal transition and metastasis in colorectal cancer by interacting with SRSF6. *Cancer Lett.*, **380**, 476–484.
33. Park,S., Brugiolo,M., Akerman,M., Das,S., Urbanski,L., Geier,A., Kesarwani,A.K., Fan,M., Leclair,N., Lin,K.T. *et al.* (2019) Differential functions of splicing factors in mammary transformation and breast cancer metastasis. *Cell Rep.*, **29**, 2672–2688.
34. Wan,L., Yu,W., Shen,E., Sun,W., Liu,Y., Kong,J., Wu,Y., Han,F., Zhang,L., Yu,T. *et al.* (2019) SRSF6-regulated alternative splicing that promotes tumour progression offers a therapy target for colorectal cancer. *Gut*, **68**, 118–129.
35. Yang,X., Zhan,P., Feng,S., Ji,H., Tian,W., Wang,M., Cheng,C. and Song,B. (2020) SRSF6 regulates alternative splicing of genes involved in DNA damage response and DNA repair in HeLa cells. *Oncol. Rep.*, **44**, 1851–1862.
36. Juan-Mateu,J., Alvelos,M.I., Turatsinze,J.V., Villate,O., Lizarraga-Mollinedo,E., Grieco,F.A., Marroqui,L., Bugliani,M., Marchetti,P. and Eizirik,D.L. (2018) SRp55 regulates a splicing network that controls human pancreatic beta-cell function and survival. *Diabetes*, **67**, 423–436.
37. Nowak,D.G., Woolard,J., Amin,E.M., Konopatskaya,O., Saleem,M.A., Churchill,A.J., Ladomery,M.R., Harper,S.J. and Bates,D.O. (2008) Expression of pro- and anti-angiogenic isoforms of VEGF is differentially regulated by splicing and growth factors. *J. Cell Sci.*, **121**, 3487–3495.
38. Dobin,A., Davis,C.A., Schlesinger,F., Drenkow,J., Zaleski,C., Jha,S., Batut,P., Chaisson,M. and Gingeras,T.R. (2013) STAR: ultrafast universal RNA-seq aligner. *Bioinformatics*, **29**, 15–21.
39. Anders,S., Pyl,P.T. and Huber,W. (2015) HTSeq—a Python framework to work with high-throughput sequencing data. *Bioinformatics*, **31**, 166–169.
40. Love,M.I., Huber,W. and Anders,S. (2014) Moderated estimation of fold change and dispersion for RNA-seq data with DESeq2. *Genome Biol.*, **15**, 550.
41. Yu,G., Wang,L.G., Han,Y. and He,Q.Y. (2012) clusterProfiler: an R package for comparing biological themes among gene clusters. *OMICS*, **16**, 284–287.
42. Vaquero-Garcia,J., Barrera,A., Gazzara,M.R., Gonzalez-Vallinas,J., Lahens,N.F., Hogenesch,J.B., Lynch,K.W. and Barash,Y. (2016) A new view of transcriptome complexity and regulation through the lens of local splicing variations. *Elife*, **5**, e11752.
43. Zhang,X.O., Dong,R., Zhang,Y., Zhang,J.L., Luo,Z., Zhang,J., Chen,L.L. and Yang,L. (2016) Diverse alternative back-splicing and alternative splicing landscape of circular RNAs. *Genome Res.*, **26**, 1277–1287.
44. Gao,Y., Zhang,J. and Zhao,F. (2018) Circular RNA identification based on multiple seed matching. *Brief Bioinform.*, **19**, 803–810.
45. Li,H. and Durbin,R. (2009) Fast and accurate short read alignment with Burrows–Wheeler transform. *Bioinformatics*, **25**, 1754–1760.
46. Huppertz,I., Attig,J., D'Ambrogio,A., Easton,L.E., Sibley,C.R., Sugimoto,Y., Tajnik,M., König,J. and Ule,J. (2014) iCLIP: protein–RNA interactions at nucleotide resolution. *Methods*, **65**, 274–287.
47. Busch,A., Bruggemann,M., Ebersberger,S. and Zarnack,K. (2020) iCLIP data analysis: a complete pipeline from sequencing reads to RBP binding sites. *Methods*, **178**, 49–62.
48. Smith,T., Heger,A. and Sudbery,I. (2017) UMI-tools: modeling sequencing errors in Unique Molecular Identifiers to improve quantification accuracy. *Genome Res.*, **27**, 491–499.
49. Krakau,S., Richard,H. and Marsico,A. (2017) PureCLIP: capturing target-specific protein–RNA interaction footprints from single-nucleotide CLIP-seq data. *Genome Biol.*, **18**, 240.
50. Bodenhofer,U., Bonatesta,E., Horejs-Kainrath,C. and Hochreiter,S. (2015) msa: an R package for multiple sequence alignment. *Bioinformatics*, **31**, 3997–3999.
51. Wagih,O. (2017) ggseqlogo: a versatile R package for drawing sequence logos. *Bioinformatics*, **33**, 3645–3647.
52. Wilks,C., Zheng,S.C., Chen,F.Y., Charles,R., Solomon,B., Ling,J.P., Imada,E.L., Zhang,D., Joseph,L., Leek,J.T. *et al.* (2021) recount3: summaries and queries for large-scale RNA-seq expression and splicing. *Genome Biol.*, **22**, 323.
53. Bhandari,V., Hoey,C., Liu,L.Y., Lalonde,E., Ray,J., Livingstone,J., Lesurf,R., Shiah,Y.J., Vujcic,T., Huang,X. *et al.* (2019) Molecular

landmarks of tumor hypoxia across cancer types. *Nat. Genet.*, **51**, 308–318.
54. Cancer,Genome Atlas Network (2012) Comprehensive molecular portraits of human breast tumours. *Nature*, **490**, 61–70.
55. Schindelin,J., Arganda-Carreras,I., Frise,E., Kaynig,V., Longair,M., Pietzsch,T., Preibisch,S., Rueden,C., Saalfeld,S., Schmid,B. *et al.* (2012) Fiji: an open-source platform for biological-image analysis. *Nat. Methods*, **9**, 676–682.
56. Alvelos,M.I., Bruggemann,M., Sutandy,F.R., Juan-Mateu,J., Colli,M.L., Busch,A., Lopes,M., Castela,A., Aartsma-Rus,A., König,J. *et al.* (2021) The RNA-binding profile of the splicing factor SRSF6 in immortalized human pancreatic beta-cells. *Life Sci. Alliance*, **4**, e202000825.
57. Müller-McNicoll,M., Botti,V., de Jesus Domingues,A.M., Brandl,H., Schwich,O.D., Steiner,M.C., Curk,T., Poser,I., Zarnack,K. and Neugebauer,K.M. (2016) SR proteins are NXF1 adaptors that link alternative RNA processing to mRNA export. *Genes Dev.*, **30**, 553–566.
58. Feng,H., Bao,S., Rahman,M.A., Weyn-Vanhentenryck,S.M., Khan,A., Wong,J., Shah,A., Flynn,E.D., Krainer,A.R. and Zhang,C. (2019) Modeling RNA-binding protein specificity in vivo by precisely registering protein–RNA crosslink sites. *Mol. Cell*, **74**, 1189–1204.
59. Krchnakova,Z., Thakur,P.K., Krausova,M., Bieberstein,N., Haberman,N., Müller-McNicoll,M. and Stanek,D. (2019) Splicing of long non-coding RNAs primarily depends on polypyrimidine tract and 5′ splice-site sequences due to weak interactions with SR proteins. *Nucleic Acids Res.*, **47**, 911–928.
60. Galganski,L., Urbanek,M.O. and Krzyzosiak,W.J. (2017) Nuclear speckles: molecular organization, biological function and role in disease. *Nucleic Acids Res.*, **45**, 10350–10368.
61. Munoz-Sanchez,J. and Chanez-Cardenas,M.E. (2019) The use of cobalt chloride as a chemical hypoxia model. *J. Appl. Toxicol.*, **39**, 556–570.
62. Koshiji,M., Kageyama,Y., Pete,E.A., Horikawa,I., Barrett,J.C. and Huang,L.E. (2004) HIF-1alpha induces cell cycle arrest by functionally counteracting Myc. *EMBO J.*, **23**, 1949–1956.
63. Müller-McNicoll,M., Rossbach,O., Hui,J. and Medenbach,J. (2019) Auto-regulatory feedback by RNA-binding proteins. *J. Mol. Cell Biol.*, **11**, 930–939.
64. Gardner,L.B. (2008) Hypoxic inhibition of nonsense-mediated RNA decay regulates gene expression and the integrated stress response. *Mol. Cell. Biol.*, **28**, 3729–3741.
65. Königs,V., de Oliveira Freitas Machado,C., Arnold,B., Blümel,N., Solovyeva,A., Löbbert,S., Schafranek,M., Ruiz De Los Mozos,I., Wittig,I., McNicoll,F. *et al.* (2020) SRSF7 maintains its homeostasis through the expression of split-ORFs and nuclear body assembly. *Nat. Struct. Mol. Biol.*, **27**, 260–273.
66. Leclair,N.K., Brugiolo,M., Urbanski,L., Lawson,S.C., Thakar,K., Yurieva,M., George,J., Hinson,J.T., Cheng,A., Graveley,B.R. *et al.* (2020) Poison exon splicing regulates a coordinated network of SR protein expression during differentiation and tumorigenesis. *Mol. Cell*, **80**, 648–665.
67. Liang,D., Tatomer,D.C., Luo,Z., Wu,H., Yang,L., Chen,L.L., Cherry,S. and Wilusz,J.E. (2017) The output of protein-coding genes shifts to circular RNAs when the pre-mRNA processing machinery is limiting. *Mol. Cell*, **68**, 940–954.
68. Wang,M., Hou,J., Müller-McNicoll,M., Chen,W. and Schuman,E.M. (2019) Long and repeat-rich intronic sequences favor circular RNA formation under conditions of reduced spliceosome activity. *iScience*, **20**, 237–247.
69. König,J., Zarnack,K., Rot,G., Curk,T., Kayikci,M., Zupan,B., Turner,D.J., Luscombe,N.M. and Ule,J. (2010) iCLIP reveals the function of hnRNP particles in splicing at individual nucleotide resolution. *Nat. Struct. Mol. Biol.*, **17**, 909–915.
70. Erkelenz,S., Mueller,W.F., Evans,M.S., Busch,A., Schoneweis,K., Hertel,K.J. and Schaal,H. (2013) Position-dependent splicing activation and repression by SR and hnRNP proteins rely on common mechanisms. *RNA*, **19**, 96–102.
71. Fu,X.D. and Ares,M. Jr (2014) Context-dependent control of alternative splicing by RNA-binding proteins. *Nat. Rev. Genet.*, **15**, 689–701.
72. Hochberg-Laufer,H., Schwed-Gross,A., Neugebauer,K.M. and Shav-Tal,Y. (2019) Uncoupling of nucleo-cytoplasmic RNA export and localization during stress. *Nucleic Acids Res.*, **47**, 4778–4797.
73. Kurogi,Y., Matsuo,Y., Mihara,Y., Yagi,H., Shigaki-Miyamoto,K., Toyota,S., Azuma,Y., Igarashi,M. and Tani,T. (2014) Identification of a chemical inhibitor for nuclear speckle formation: implications for the function of nuclear speckles in regulation of alternative pre-mRNA splicing. *Biochem. Biophys. Res. Commun.*, **446**, 119–124.
74. Hasenson,S.E. and Shav-Tal,Y. (2020) Speculating on the roles of nuclear speckles: how RNA–protein nuclear assemblies affect gene expression. *Bioessays*, **42**, e2000104.
75. Chujo,T., Yamazaki,T., Kawaguchi,T., Kurosaka,S., Takumi,T., Nakagawa,S. and Hirose,T. (2017) Unusual semi-extractability as a hallmark of nuclear body-associated architectural noncoding RNAs. *EMBO J.*, **36**, 1447–1462.
76. Liao,S.E. and Regev,O. (2021) Splicing at the phase-separated nuclear speckle interface: a model. *Nucleic Acids Res.*, **49**, 636–645.
77. Guo,K., Searfoss,G., Krolikowski,D., Pagnoni,M., Franks,C., Clark,K., Yu,K.T., Jaye,M. and Ivashchenko,Y. (2001) Hypoxia induces the expression of the pro-apoptotic gene BNIP3. *Cell Death Differ.*, **8**, 367–376.
78. Fonseca,C.L., Malaby,H.L.H., Sepaniac,L.A., Martin,W., Byers,C., Czechanski,A., Messinger,D., Tang,M., Ohi,R., Reinholdt,L.G. *et al.* (2019) Mitotic chromosome alignment ensures mitotic fidelity by promoting interchromosomal compaction during anaphase. *J. Cell Biol.*, **218**, 1148–1163.
79. Weigand,J.E., Boeckel,J.N., Gellert,P. and Dimmeler,S. (2012) Hypoxia-induced alternative splicing in endothelial cells. *PLoS One*, **7**, e42697.
80. Greig,J.A., Nguyen,T.A., Lee,M., Holehouse,A.S., Posey,A.E., Pappu,R.V. and Jedd,G. (2020) Arginine-enriched mixed-charge domains provide cohesion for nuclear speckle condensation. *Mol. Cell*, **77**, 1237–1250.
81. Ilik,I.A., Malszycki,M., Lubke,A.K., Schade,C., Meierhofer,D. and Aktas,T. (2020) SON and SRRM2 are essential for nuclear speckle formation. *Elife*, **9**, e60579.
82. Hochberg-Laufer,H., Neufeld,N., Brody,Y., Nadav-Eliyahu,S., Ben-Yishay,R. and Shav-Tal,Y. (2019) Availability of splicing factors in the nucleoplasm can regulate the release of mRNA from the gene after transcription. *PLoS Genet.*, **15**, e1008459.
83. Gilkes,D.M., Semenza,G.L. and Wirtz,D. (2014) Hypoxia and the extracellular matrix: drivers of tumour metastasis. *Nat. Rev. Cancer*, **14**, 430–439.
84. Welch,D.R. and Hurst,D.R. (2019) Defining the hallmarks of metastasis. *Cancer Res.*, **79**, 3011–3027.
85. Spill,F., Reynolds,D.S., Kamm,R.D. and Zaman,M.H. (2016) Impact of the physical microenvironment on tumor progression and metastasis. *Curr. Opin. Biotechnol.*, **40**, 41–48.
86. Jensen,M.A., Wilkinson,J.E. and Krainer,A.R. (2014) Splicing factor SRSF6 promotes hyperplasia of sensitized skin. *Nat. Struct. Mol. Biol.*, **21**, 189–197.
87. Parrilla,A., Cirillo,L., Thomas,Y., Gotta,M., Pintard,L. and Santamaria,A. (2016) Mitotic entry: the interplay between Cdk1, Plk1 and Bora. *Cell Cycle*, **15**, 3177–3182.
88. Vigneron,S., Sundermann,L., Labbe,J.C., Pintard,L., Radulescu,O., Castro,A. and Lorca,T. (2018) Cyclin A-cdk1-dependent phosphorylation of Bora is the triggering factor promoting mitotic entry. *Dev. Cell*, **45**, 637–650.
89. Karni-Schmidt,O., Lokshin,M. and Prives,C. (2016) The roles of MDM2 and MDMX in cancer. *Annu. Rev. Pathol.*, **11**, 617–644.
90. Mancini,F., Teveroni,E., Di Conza,G., Monteleone,V., Arisi,I., Pellegrino,M., Buttarelli,M., Pieroni,L., D'Onofrio,M., Urbani,A. *et al.* (2017) MDM4 actively restrains cytoplasmic mTORC1 by sensing nutrient availability. *Mol. Cancer*, **16**, 55.
91. Matijasevic,Z., Krzywicka-Racka,A., Sluder,G., Gallant,J. and Jones,S.N. (2016) The Zn-finger domain of MdmX suppresses cancer progression by promoting genome stability in p53-mutant cells. *Oncogenesis*, **5**, e262.
92. Wohlberedt,K., Klusmann,I., Derevyanko,P.K., Henningsen,K., Choo,J., Manzini,V., Magerhans,A., Giansanti,C., Eischen,C.M., Jochemsen,A.G. *et al.* (2020) Mdm4 supports DNA replication in a p53-independent fashion. *Oncogene*, **39**, 4828–4843.
93. Moggs,J.G., Grandi,P., Quivy,J.P., Jonsson,Z.O., Hubscher,U., Becker,P.B. and Almouzni,G. (2000) A CAF-1–PCNA-mediated chromatin assembly pathway triggered by sensing DNA damage. *Mol. Cell. Biol.*, **20**, 1206–1218.

94. Kadkova,A., Radecke,J. and Sorensen,J.B. (2019) The SNAP-25 protein family. *Neuroscience*, **420**, 50–71.
95. Chen,M., Qiu,T., Wu,J., Yang,Y., Wright,G.D., Wu,M. and Ge,R. (2018) Extracellular anti-angiogenic proteins augment an endosomal protein trafficking pathway to reach mitochondria and execute apoptosis in HUVECs. *Cell Death Differ.*, **25**, 1905–1920.
96. Markolin,P., Davidson,N., Hirt,C.K., Chabbert,C.D., Zamboni,N., Schwank,G., Krek,W. and Rätsch,G. (2020) Characterization of HIF-dependent alternative isoforms in pancreatic cancer. bioRxiv doi: http://dx.doi.org/10.1101/826156, 14 February 2020, preprint: not peer reviewed.
97. Thomas,J.D., Polaski,J.T., Feng,Q., De Neef,E.J., Hoppe,E.R., McSharry,M.V., Pangallo,J., Gabel,A.M., Belleville,A.E., Watson,J. *et al.* (2020) RNA isoform screens uncover the essentiality and tumor-suppressor activity of ultraconserved poison exons. *Nat. Genet.*, **52**, 84–94.